IN-SITU SYNCHROTRON X-RAY AND MICRO-COMPUTED TOMOGRAPHY OF NONWOVEN ARAMIDS: DEFORMATION MECHANISMS

A Thesis

Presented to the Faculty of the Graduate School

of Cornell University

In Partial Fulfillment of the Requirements for the Degree of

Master of Science

by

Simge Uzun

January 2017

ABSTRACT

Nonwoven materials have attracted much interest in the industry due to their high surface area, high porosity, and low cost. However due to the complexity of deformation mechanisms in these materials, controlling the mechanical properties has been challenging. Therefore, it is important to establish the fundamental understanding of the relationship between the microstructure and the macroscopic behavior. Motivated by this, mechanical properties and deformation mechanisms of aramid nonwovens as a function of areal weight were reported using several analytical tools. The initial fiber orientation alignment was found significantly different within the nonwoven types according to XRD patterns. Fiber orientation evolution under both monotonic tensile and stress relaxation tests was tracked using in-situ X-ray diffraction. As the strain increased, fiber alignment along the loading direction was observed in all three types of nonwovens. Results suggested that the areal weight is not necessarily a predictor of the mechanical properties of aramid nonwovens as the fiber alignment plays a vital role in the performance of these materials.

BIOGRAPHICAL SKETCH

Simge Uzun is a candidate for graduation upon defense of her master's thesis. She has completed her undergraduate degree in textile engineering at Istanbul Technical University, Turkey. During her undergraduate program, she also had the chance to participate in the EU-Erasmus Exchange Program and spend one semester in the mechanical engineering department at Dresden University of Technology, Germany.

At Cornell, she has improved her research skills through several projects. One early project involved operating an industrial-sized extruder to produce polymer-based nonwoven materials. She also explored the use of nanofibers to generate tubular and self-sustained porous structures. Her research experience at Cornell involved multiple side-projects that enabled her to widen her understanding in the field of polymeric fibers as well as enabled her to improve her individual research capabilities by gaining hands on experience in various laboratory equipments. Her master's thesis strengthened her computational skills as it focused on structural analysis and fiber orientation evolution under deformation of aramid nonwoven materials where she developed codes necessary to analyze the XRD data to understand the microstructure at the high intensity X-Ray source at the Cornell High Energy Synchrotron Source (CHESS). She also monitored 3D microstructure changes of the aramid nonwoven specimens, induced by deformation, using in-situ micro-computed tomography imaging. These valuable research experiences enabled her to become more confident in her research.

To my parents, for their continued love and support.

ACKNOWLEDGMENTS

I would like to acknowledge my advisors, professor Juan Hinestroza and Meredith N. Silberstein, for providing me support, motivation, and guidance throughout my master's degree. Besides my advisors, I owe thanks to number of colleagues regarding research: Marion Schelling and Naigeng Chen for the assistance in CHESS experiments and insightful discussions, Meenakshi Sundaram Manivannan for the computational data analysis, Diego Alzate Sanchez for the discussions regarding chemistry related topics, Tugce Figen Kukul and Merve Ascioglu for the assistance in 3D modeling of the experimental setup. I greatly appreciate all the ideas and helpful hands contributed by each of you. I would also like to acknowledge a number of people on Cornell staff, including Karen Steffy and Xia Zeng. I appreciate the technical support from CHESS staff scientists, special thanks to Rong Huang and Zachary A. Brown for experimental hardware setup. I also thank Rob Woudman from Teijin Aramid and Jami June from TFP Ltd for providing fiber and nonwoven materials, respectively.

A huge thanks to my Turkish and American family: I cannot express enough gratitude for the support you have given me. I am very fortunate to have each of you in my life, and appreciate your tireless support and encouragement every single day. I owe a debt of gratitude to my American family, to whom I dedicated this thesis and who have been made possible my journey in USA since 2008. To Bilge, Chase, Liam and Ema: you are the best sister and brothers anyone could hope for. Bilen, you have been a wonderful boyfriend to me. I cannot say enough about the unfailing support, continuous

encouragement and friendship I have received from my boyfriend, whom I dearly love and also dedicate this thesis to.

TABLE OF CONTENTS

LIST OF FIGURES

LIST OF TABLES

CHAPTER 1

INTRODUCTION

Nonwovens are fibrous materials that are made without using weaving, knitting or braiding processes. Due to their lower manufacturing costs in comparison to woven materials, the demand for these materials is increasing, and they are used in a variety of different applications such as fireproof layers, geotextiles, ballistic protection, thermal insulation and liquid-absorbing textiles[1].

Mechanics of nonwovens are complex due to the random and entangled nature of the fiber distribution. Hence the evolution of fiber orientation under straining is not yet well understood[2]. The relationship between the macroscale mechanical behavior and the nonwoven microstructure needs to be studied and optimized in order to interpret and improve the mechanical performance of the nonwovens[3,4]. Mechanics of nonwovens is affected by a combination of many micro mechanisms such as fiber reorientation, bond failure, and fiber fracture. Nature of the interfiber bonds and their interactions with each other as well as the initial structure of nonwoven have an impact on the microscopic and macroscopic mechanical properties[5].

Evolution of microstructure during deformation provides important information for understanding nonwoven mechanics. X-ray diffraction (XRD) experiments on nonwoven

materials with crystalline fibers are used to track orientation distribution changes. The fiber orientation evolution of a needle punched polyethylene nonwoven[5] and polypropylene nonwoven[6] was explained through XRD experiments in recent publications. Another powerful technique for analyzing the microstructure of nonwovens is micro-computed tomography (μCT), which produces 3-dimensional (3D) image of the material and has been used for many types of nonwovens, such as paper[7], needle-punched[8], point-bonded[9] and thermally-bonded[6] nonwovens. These studies report on the changes in the structural parameters upon deformation.

The aim of this study is to analyze the deformation mechanism of series of aramid nonwoven specimens as a function of their areal weight. Using synchrotron radiation, microstructural changes of nonwoven under uniaxial tensile loading were imaged. Distribution of fiber orientation was then computed to depict the fiber realignment process quantitatively. In particular, μCT was used to visualize the 3D deformation mechanism of nonwovens at specified strains including the elastic, pre-, and post-yield regions. Furthermore, XRD experiments were used to track gradual fiber orientation variation in both monotonic tensile and stress relaxation tests. Detailed analysis was conducted by the combination of a number of experimental techniques to determine the macroscopic mechanical behavior (uniaxial tensile tests) and the microstructure evolution through synchrotron radiation (XRD and μCT).

CHAPTER 2

MATERIALS

The Technical Fiber Products (TFP) Global Ltd. aramid nonwoven specimens investigated are composed of para-aramid staple fibers supplied from Teijin Twaron and a binder. Binder is a thermoplastic polyester solution cross-linked with melamine formaldehyde. The staple fibers were produced by dry-jet wet-spinning process. The fibers have a reported diameter of 12 μm and a length of 12 mm, which was later confirmed using field emission scanning electron microscopy (FESEM). Table 1 shows the areal weight for three different aramid nonwoven specimens selected for the experiments and their specifics.

Table 1: Material properties of the investigated aramid nonwoven specimens.

Specimen	Areal Weight (g/m^2)	Thickness (mm)
A14	14	0.20 ± 0.002
A34	34	0.57 ± 0.005
A50	50	0.76 ± 0.008

Lowest areal weight (14 g/m^2), intermediate areal weight (34 g/m^2) and highest areal weight (50 g/m^2) materials were referred as A14, A34 and A50, respectively. FAST-1

compression meter was used for the thickness measurements of nonwoven specimens. Ten measurements were recorded from different parts of the nonwoven for each type of material under a pressure of 9.81 kPa and average of ten thickness measurements were reported in Table 1.

2.1. Aramid fiber properties

2.1.1. Manufacturing of aramid fiber

Aramid (short for aromatic polyamide) is described as “a manufactured fiber that consists of a long-chain synthetic polyamide in which at least 85% of the amide linkages are attached directly to two aromatic rings” by the US Federal Trade Commission in 1974[10]. Poly(p-phenylene terephthalamide) abbreviated PPTA fibers are widely used in textile and advanced composites. Twaron is a commercial version of the PPTA aramid fiber, supplied by Teijin. The chemical structure, the synthesis and the structure of PPTA fiber are shown in Figure 1, 2, 3, respectively.

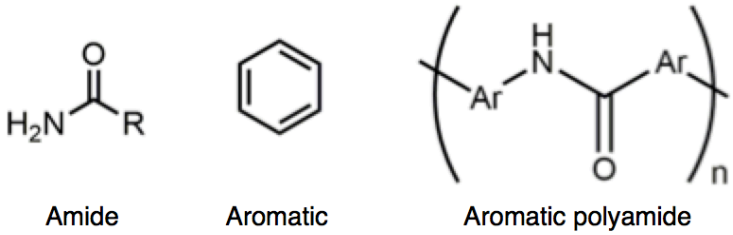

Figure 1: Chemical structure of PPTA fiber.

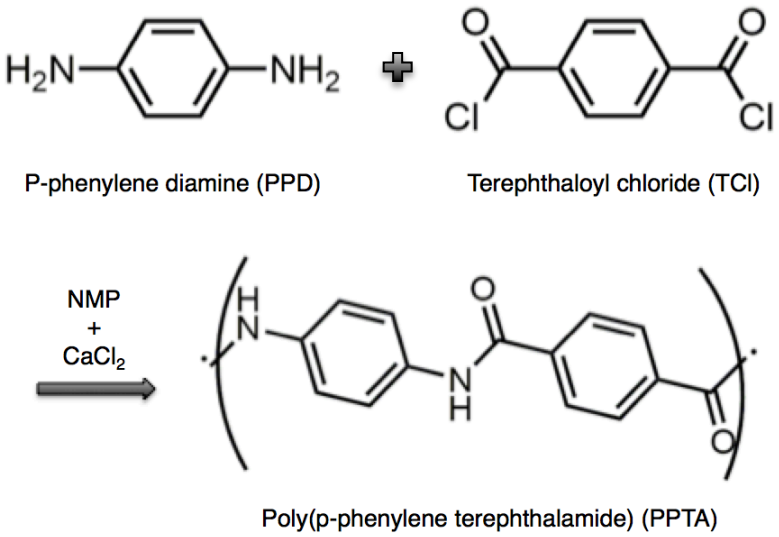

Figure 2: Synthesis of poly (p-phenylene terephthalamide).

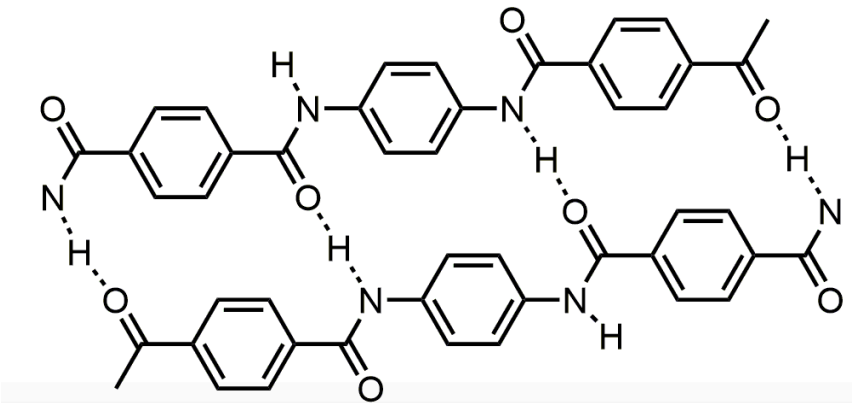

Figure 3: Structure of poly (p-phenylene terephthalamide).

PPTA is a product of p-phenylene diamine (PPD) and terephthaloyl chloride (TCl). The polycondensation was carried out in N-methyl pyrrolidone (NMP), which contains dissolved calcium chloride ($CaCl_2$). $CaCl_2$ was used as an ionic component due to its capability to coordinate with the hydrogen bonds of the amide groups[11,12].

H. Blades[13] discovered that the high-strength and high-modulus fibers can be spun from anisotropic solutions of aramid polymers by using dry-jet wet-spinning process (as shown in Figure 4). The synthesized PPTA was dissolved in a solvent and processed into a PPTA fiber by using dry-jet wet-spinning. In this step, 100% anhydrous concentrated sulfuric acid (H_2SO_4) at 80 C° was used as the solvent of spinning solution because PPTA is not readily soluble in organic solvents. The solution state corresponds to a nematic liquid crystalline state between a polymer concentration of about 10wt% and 20wt%. Solution temperature and polymer concentration affect the degree of orientation of the polymer chains.

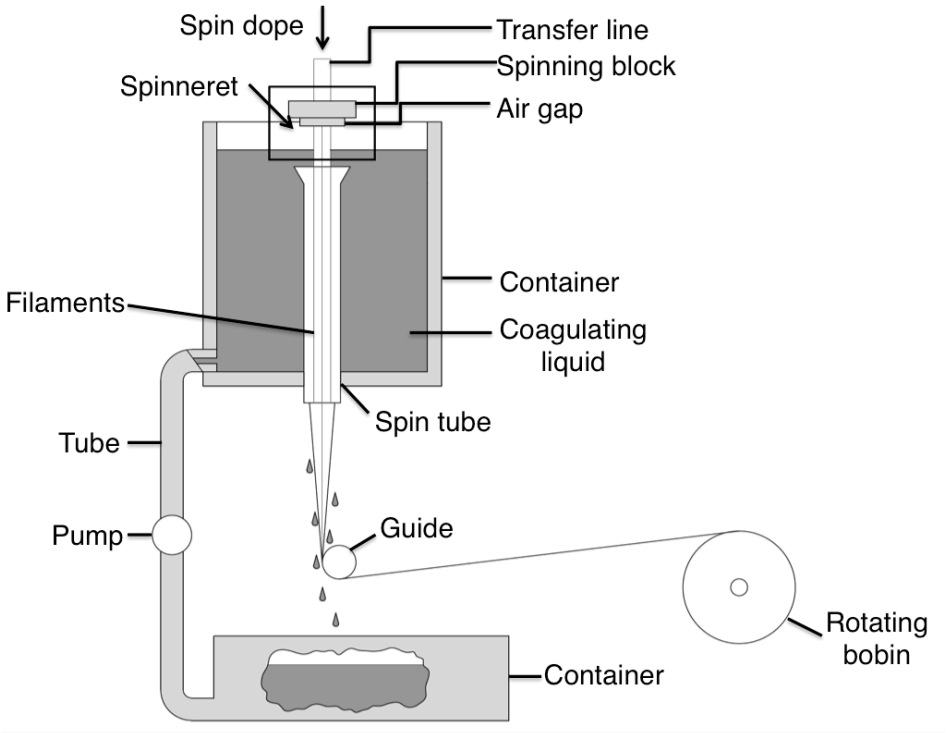

Figure 4: Dry-jet wet-spinning process by Blades[12-14].

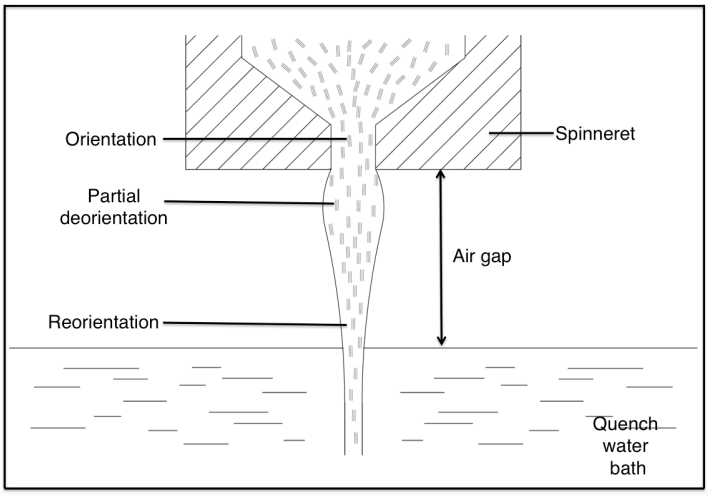

Figure 5: PPTA fiber formation[15-17].

The polymer spinning solution (liquid crystal domains) was extruded through the spinneret and exposed to elongational stretch across about 0.5 to 1cm of the air gap[18,19]. Higher degree of molecular orientation was obtained due to the air gap as shown in Figure 5. Crystal domains elongated and oriented in the direction of deformation under shear[20-22]. The crucial fiber microstructure formation takes place during the coagulation stage of this spinning process. Higher polymer orientation in the coagulation bath leads to higher mechanical properties of the fiber. The final stages of the spinning process for the coagulated filaments consist of washing, neutralizing and drying.

2.1.2. General properties of the aramid fibers

The form and the structure of the fiber represent fiber morphology, which includes the molecular arrangement of individual molecules and groups of molecules within the fiber.

The PPTA polymer chains are very stiff due to bonding of rigid phenylene rings in para position. There are amide groups along the linear macromolecular backbone, which allows extensive hydrogen bonding between adjacent chains and causes efficient chain packing and high crystallinity[23,24]. Northolt et al. investigated the PPTA fiber's structure on the basis of X-ray diffraction and claimed that the PPTA fiber has a paracrystalline structure instead of having a two- phase structure consisting of amorphous and crystalline domains[25].

The Twaron aramid fiber has an anisotropic structure. Fibrils are extended chains of molecules and they are randomly interconnected at "tie points". Intra-molecular covalent bonds hold the individual atoms together which constitutes the polymer chains. Secondary bonds such as hydrogen bonds and van der Waals forces also exist[26]. Yang et al.[15] reported that the equatorial XRD scan gives peaks at diffraction angles 2θ (i.e. Bragg angles) of 20.5°, 23° and 28.2° corresponding to crystalline planes aligned in (110), (200) and (211) directions, respectively.

PPTA fibers have good thermal stability and their mechanical properties, such as high elastic modulus, high strength, low elongation at break, and high stability at elevated temperatures are quite remarkable when compared to conventional synthetic fibers. Aramid fibers produced with dry-jet wet-spinning technique have an initial modulus of ca. 70 GPa, which can be improved by short-term heating under tension to ca. 140 GPa [15,27,28].

Most organic solvents and aqueous salt solutions have minimal effect on the mechanical properties of PPTA fibers under moderate conditions[15]. On the other hand, strong acids and bases as well as water at high temperature and high pressure can damage PPTA fibers[15,29,30]. Moreover, thermo gravimetric analysis (TGA) is used to determine the decomposition temperature (T_d) of these fibers and showed that PPTA fibers are thermally stable up to about 550 °C[31].

2.2. Aramid nonwoven properties

The applications of nonwoven materials are determined by their mechanical, physical and chemical properties. Critical properties such as fiber diameter, fiber orientation in the fiber network, pore size, and areal weight have an influence on the performance of the nonwovens[32]. Understanding the nonwoven properties would be a great help to investigate how fiber properties translate into fiber networks.

2.2.1. Manufacturing of aramid nonwoven materials

Nonwoven specimens used in this investigation were produced using wet-laid process. Dexter Inc. initially developed this process in the 1930s, and then the company was purchased by Ahlstrom Inc. in 2000. Ahlstrom is one of the main producers of wet-laid products today[32]. There are not so many companies which use wet-laid process since it requires high capital investment and vast amount of water[1,32].

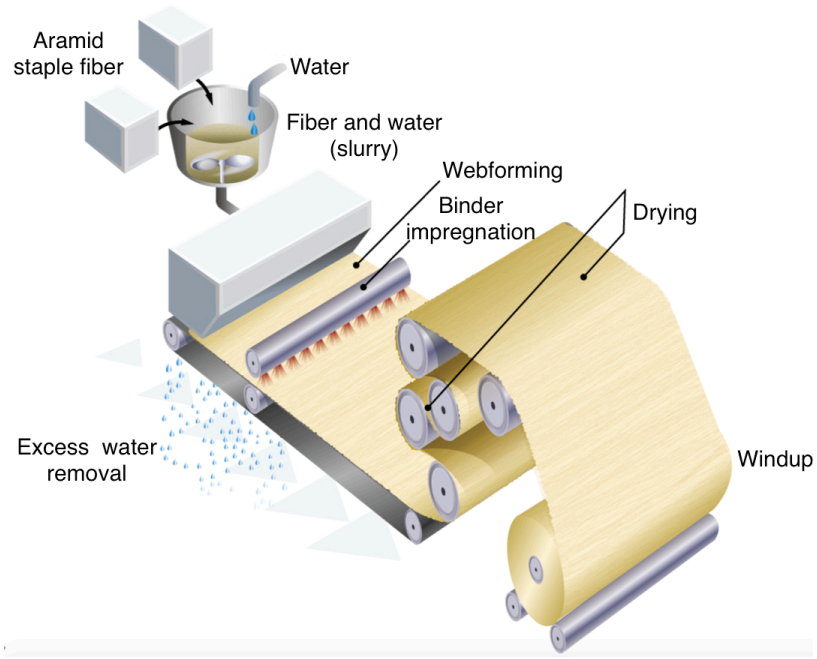

Figure 6: Wet-laid process[33].

Figure 6 demonstrates the wet-laid process, which consists of three main stages. The first one requires the swelling and dispersion of the fiber in water and then the transfer of the suspension onto a continuous travelling screen. The second stage would be continuous web formation on the screen by filtration. Lastly, drying and bonding of the web would take place. One of the main advantages of the wet-laid process is the capability to use various types of fibers[32]. Any kind of staple fibers that can disperse in water can be used with this technique, including aramid fibers, leather, glass, ceramics and even stainless steel[1,32]. The fibers are randomly oriented in the web, thus the strength of such a web is theoretically similar in all directions.

CHAPTER 3

EXPERIMENTAL

Mechanical properties and deformation mechanisms of single aramid fiber and aramid nonwoven specimens as a function of areal weight using several analytical tools were studied. X-ray diffraction (XRD) experiments combined with uniaxial mechanical testing were used to investigate the micromechanical mechanisms governing nonwoven strength. The areal weight effect on the fiber orientation distribution change during monotonic tensile and stress relaxation test was carried out by in-situ XRD experiments. Field emission scanning electron microscope (FESEM) was used to characterize the structural and morphological properties of nonwoven specimens. Microstructure changes during deformation was imaged using synchrotron micro-computed tomography (μCT). Fiber-binder ratio in the nonwoven materials was analyzed by using thermogravimetric analysis (TGA).

3.1. Characterization of mechanical behavior

Uniaxial tensile measurements were performed by Zwick/Roell Z010 tensile testing system using a 10kN and 20N load cell with pneumatic grips for nonwoven specimens and single aramid fibers, respectively. The mechanical response of constituent fibers was studied to obtain a better understanding of the mechanics of nonwoven specimens under uniaxial tensile loading.

All fiber and nonwoven samples were stored in opaque black bags and closed cabinets in order to limit exposure to light and UV radiation. Rectangular nonwoven specimens with the dimensions of 9 x 45 mm were tested with a gauge length set at 27 mm. Nonwoven mats were received in a letter-size sheet format from the manufacturer where the mats were made with the machine direction being along the longest sheet dimension. Single aramid fibers were mounted across a cardboard window using Future glue®. Gauge length of the fiber was set to 6 mm, and the fiber-mounted cardboard was placed within the grips of the tensile tester and the two ends separated after carefully cutting both sides of the cardboard window. Care was taken to ensure that the fibers were mounted with negligible glue to a sample holder to prevent the glue penetration to the fiber. No evidence of grip slippage was noted.

Engineering strain was calculated by dividing the crosshead displacements with the original gauge length of 27 mm and 6 mm for the nonwoven and fiber specimens, respectively. Each specimen was weighed three times and the average of three measurements was used as the weight of the specimen, then its weight that falls into the gauge length area was calculated and used for the specific force calculations. Average of ten thickness measurements was used for engineering stress calculations.

Monotonic tensile tests in the machine and transverse directions were carried out at a constant strain rate of 0.00588 s^{-1} in order to investigate the mechanical anisotropy of the aramid nonwoven specimens. For each measurement point, the average value of

five samples was used for nonwoven specimens and four samples were used for single fiber specimens in order to consider specimen-dependent variation. A measurement was considered valid whenever the tensile fracture did not occur near the clamps. From specific force - engineering strain curves, the mechanical properties such as scaled modulus, scaled strength, and failure strain were determined. Young's modulus was calculated from engineering stress - engineering strain curves. Both moduli were defined as the slope of the specified curve measured in strain range of 0 - 0.8% and measured in kN/g and MPa for scaled modulus and Young's modulus, respectively.

The stress relaxation tests demonstrate strain rate dependency of stress. Stress relaxation is alternative and facile way of measuring time dependence of stress. Relaxation behavior of nonwovens was investigated by stretching at a constant strain rate of 0.00588 s^{-1}, 0.0588 s^{-1} and 0.588 s^{-1} to an engineering strain of 0.01 and holding at constant strain for 10 mins. Individual fibers were only loaded at a constant strain rate of 0.00588 s^{-1} due to the fiber slippage at higher strain rates. An average value of seven samples was used for each measurement point in testing all cases. Fiber and nonwoven specimens were prepared by the same procedure as in the monotonic tensile test. Decay in amplitude starting from peak force (F_{peak}) to stable force at 600 s (F_{600}) was measured for each specimen in order to understand the stress relaxation of single fiber and nonwoven specimens. Short relaxation time constant was obtained by fitting the stretched exponential function to the normalized stress relaxation curve[34].

3.2 Microstructure analysis

The microstructure of the aramid fiber and nonwoven specimens was investigated in detail by using FESEM, synchrotron μCT, and TGA. Microstructure of nonwoven specimens was first characterized by using FESEM in order to understand the qualitative binder distribution and failure mechanism of the nonwoven specimens at the fracture surface. Synchrotron μCT experiments provided further insight into the 3D microstructure and the deformation mechanisms of nonwoven specimens. Finally, TGA was used to determine the fiber-to-binder ratio in the nonwoven specimens.

3.2.1 Field emission scanning electron microscope

A Zeiss-LEO 1550 FESEM operated at 2.5 keV was used to monitor the morphology of the fiber network under various magnifications. Nonwoven specimens were coated with gold-palladium using a vacuum sputter coater to improve the conductivity of the samples, and therefore the quality of the FESEM images. The diameter of the fibers was determined from the FESEM images using the image analysis software called Fiji, Image J[35]. A measurement of fifty random fibers was used to determine the average fiber diameter. Distribution of the binder was also studied qualitatively. A qualitative indication of the nonwoven failure can be obtained from FESEM photographs. Therefore, fracture surface of the post broken nonwoven specimens were imaged to visually report the deformation trend.

3.2.2 Synchrotron micro-computed tomography

X-ray studies were carried out at the Cornell High Energy Synchrotron Source (CHESS) on beamline F3. The incident X-ray beam energy was set to 10 keV (λ=1.2398 Å) for the μCT experiment with a Si(111) double crystals monochromator. At the end, the energy bandwidth was on the order of 10^4. The second Si(111) crystal was replaced with 5° miscut Si(111) crystal to increase the size of the incident beamspot on the specimen and allow for a larger imaging region. A custom-built dual actuator load frame[6] was used at the F3 beamline for in-situ deformation during the μCT experiments.

In-situ μCT imaging was used to monitor the changes in the 3D microstructure of the nonwoven specimens. Figure 7 shows the experimental setup used during the experiment. The X-ray beamsize was 7 mm by 7 mm. In order to convert the attenuated X-ray beam into absorption contrast radiographs, a LSO:Tb scintillator, a lens system and an Andor Neo 5.5 sCMOS detector were used. The specimen was rotated 180° about the loading axis in 0.25° steps, which generated 721 radiographs in total. The exposure time was 1 s for each radiograph. Beam profile and dark images were taken using the same exposure time while the shutter was open and close, respectively. In order to minimize the morphology change, 5 mins of relaxation time was added before each scan. Nonwoven specimens were stretched in a gradual manner to strains of 0, 0.01, 0.02, 0.025, 0.03 and 0.035. A scan was carried out at each of the 6 constant strains. Two specimens of A50 nonwoven were tested during this experiment in order to

visualize the deformation under straining.

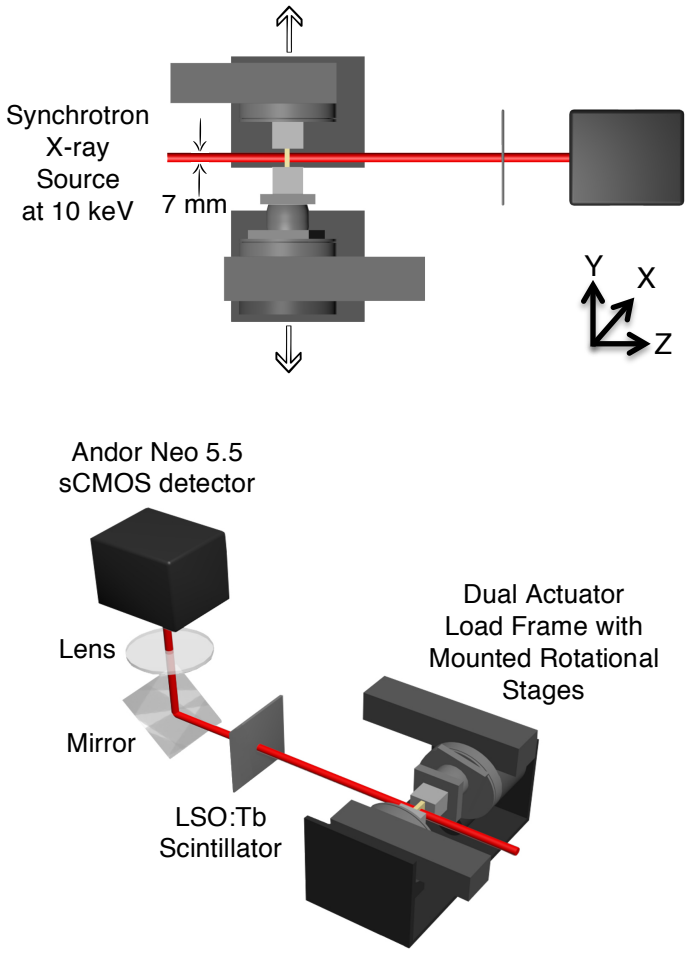

Figure 7: Schematic diagrams of in-situ µCT experimental setup. The load frame stretches the specimen to a specific strain and then rotates the specimen 180° as absorption radiographs from the incident synchrotron beam are recorded with a sCMOS detector.

A similar approach as described in our recent publication[6] was employed to construct the radiographs. The commercial software Octopus[36] was used to stack the raw radiographs, beam profile and dark images into a cross-sectional slice. Each slice consisted of 1000 pixels by 1000 pixels with a pixel size of 6.5 µm. Image denoising and

data visualization were performed with another commercial software known as AVIZO Fire[37].

3.3.3. Thermogravimetric analysis

TGA continuously measures the mass of a sample subjected to a steady increase of temperature. The measurements of the Twaron as received aramid fibers and nonwoven specimens were performed on a Q500 TGA from 25 to 1000°C at a heating rate of 5°C/min under nitrogen flow of 60mL/min. Three samples for each type of nonwoven type and two samples for aramid fibers are tested. The fiber-to-binder ratio of the nonwoven specimens was obtained by TGA analysis.

3.4. Synchrotron X-ray diffraction

Fiber orientation during deformation of the aramid nonwovens was investigated by in-situ XRD experiments. In-situ XRD experiments were carried out at the CHESS on beamline F3. Same custom-built dual actuator load frame[6] and X-ray beam energy (10 keV) were used during XRD experiments as in the μCT experiments described in Section 3.2.2. Figure 8 shows the experimental setup used during the experiment. The X-ray beamsize was set to 1 mm by 1 mm. PILATUS3 R 200K detector was used to capture the diffraction patterns. The distance between detector and the specimen was set to 70 mm.

Single aramid fiber and nonwoven specimen preparation was the same as described in Section 3.1.1. Diffraction patterns of aramid fibers at five different strains were taken before the loading experiments. The diffraction patterns showed that the location of the diffraction peaks for single fibers did not change their location under deformation. During uniaxial and relaxation tensile tests, a series of XRD patterns with an exposure time of 1 s were recorded. Both tests were carried out at a constant strain rate of 0.00147 s^{-1}. The specimens were stretched to failure during the uniaxial tensile tests. For relaxation tests, specimens were stretched to an engineering strain of 0.01 and held at a constant strain for 10 mins.

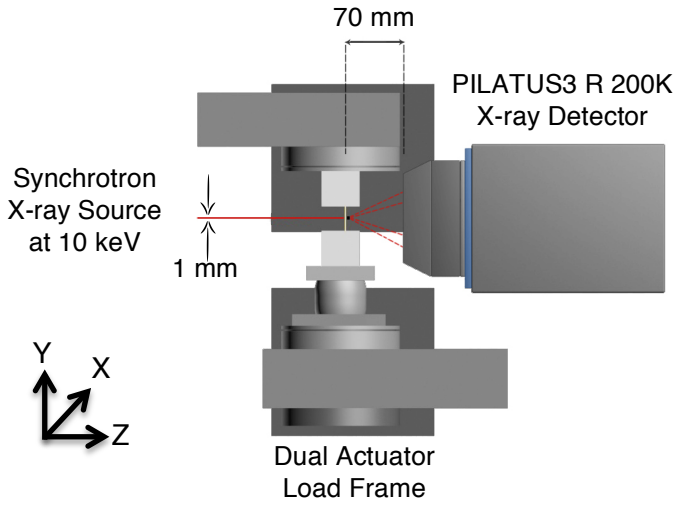

Figure 8: Schematic diagram of in-situ XRD experimental setup. The load frame stretches the specimen continuously as diffraction patterns from the incident synchrotron beam are recorded on an X-ray detector.

Fibers have different diffraction patterns depending on their orientation in the nonwoven within the diffraction volume. The resulting XRD patterns present the cumulative of the diffraction from each of the individual fibers. The orientation distribution function can be

calculated by analyzing the intensity distribution of diffraction rings. Higher the intensity on the diffraction ring higher the alignment of the fibers at the specified angle.

The ensemble averaged orientation parameter (p) was used to investigate the realignment process during deformation quantitatively.

$$p = 2 < cos^2\alpha > -1 \qquad \text{Eq. 1}$$

where α is the angle between fiber axis and loading axis (machine direction). Orientation parameter is equal to 0 when fibers are randomly oriented. If all fibers are aligned perpendicular to loading axis p will be -1. If all the fibers are aligned along loading axis p will be 1. Matlab R2015a[38] was used to process and analyze images.

CHAPTER 4

RESULTS AND DISCUSSION

4.1. Nonwoven mechanical behaviors

Monotonic tensile tests were carried out for three types of nonwoven specimens along the machine direction (MD) and the transverse direction (TD) in order to examine the anisotropic nature of the nonwoven specimens. Engineering strain – force and engineering strain – specific force curves of each type of nonwoven specimen in both machine and transverse direction are shown in Figure 9. Two representative curves for each type of the specimens at the specified directions are presented demonstrating the maximum and the minimum values obtained from the tests. All of the tests conducted fall between the shaded areas for their respective plots. The variation in mechanical response from specimen to specimen is expected considering the inherent properties of nonwovens. The overall tensile behavior observed for aramid nonwovens used in this investigation is elastic-plastic under monotonic tensile loading. Each type of nonwoven has similar strain – force and strain – specific force curve shapes. All types of specimens behave qualitatively similarly in the post-peak specific force failure region and they all demonstrate a long linear region followed by a sharp decrease in force passing the peak force. A14 (lowest areal weight) specimens seem to have higher scaled strength in the transverse direction than in the machine direction. On the other hand, intermediate areal weight (A34) specimens show higher scaled strength in the

machine direction than in the transverse direction. A50 (highest areal weight) specimens behave similarly to the A34 showing higher scaled strength in the machine direction as well. Therefore, experimental results indicate that all nonwoven types used in this study show anisotropic behavior with different scaled strength in the machine and transverse directions.

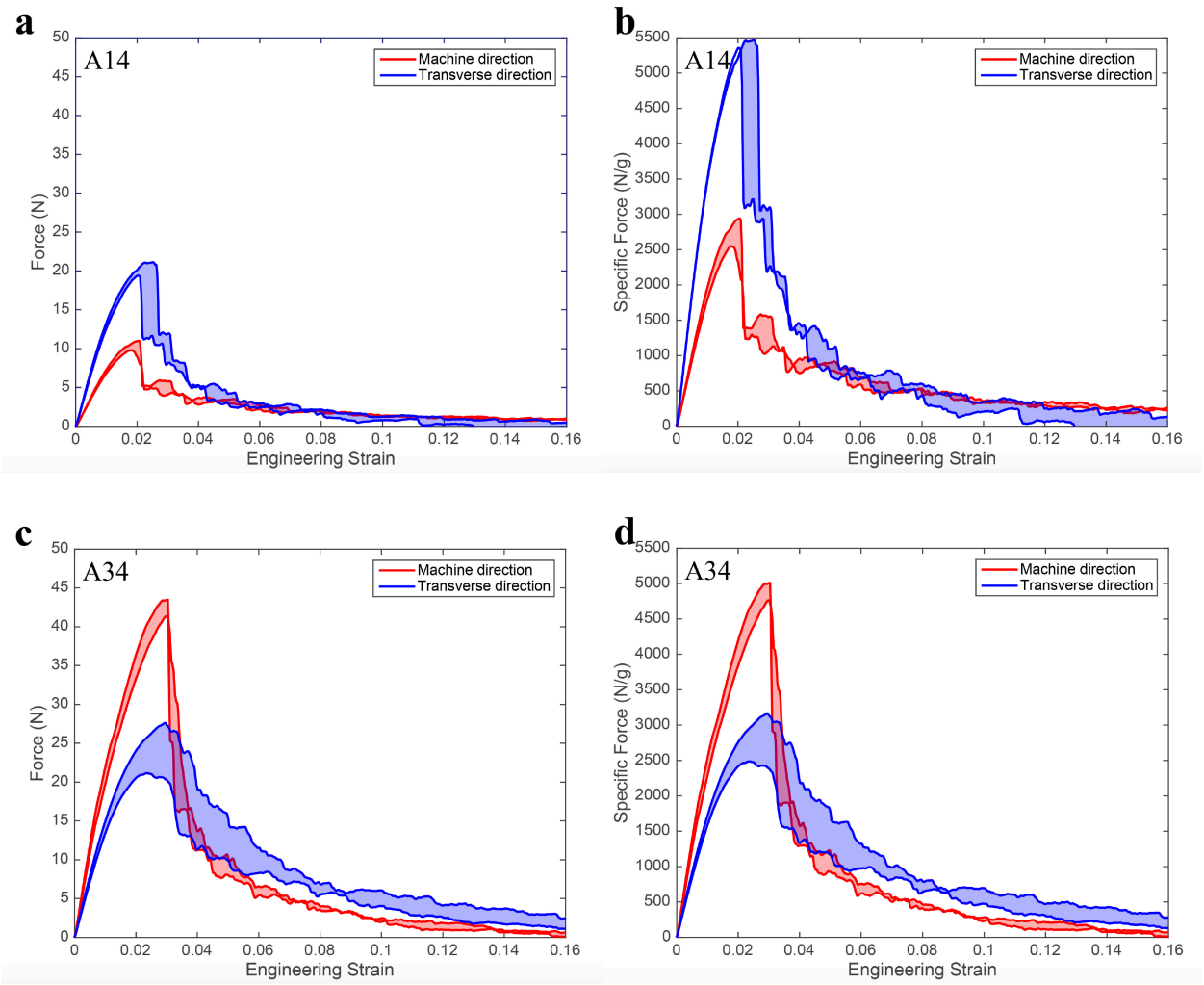

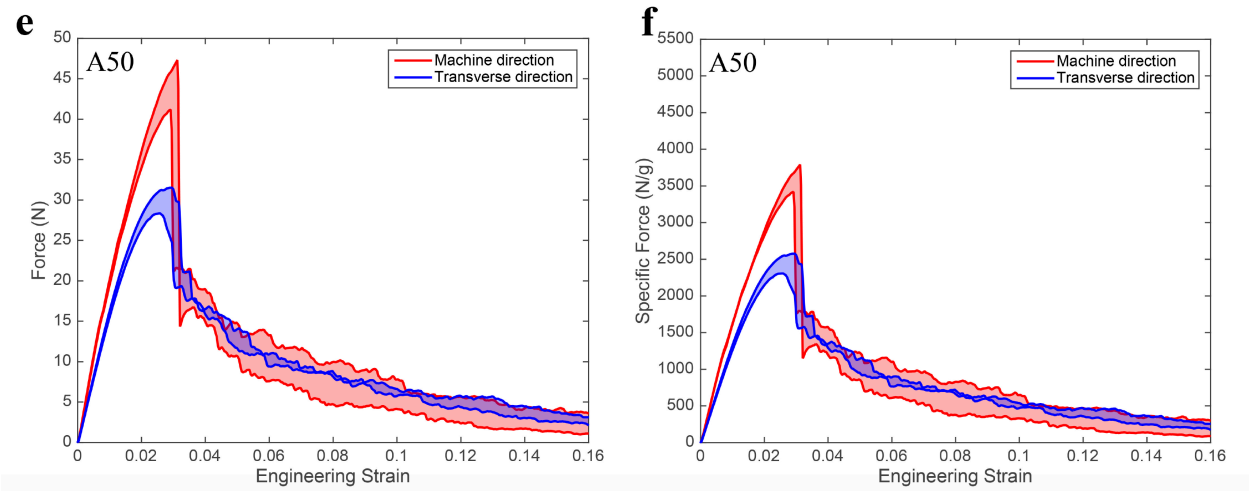

Figure 9: Monotonic tensile behavior of three types of nonwovens at a constant strain rate of 0.00588 s^{-1}. Engineering strain – force of (a) A14, (c) A34 and (e) A50. Engineering strain – specific force of (b) A14, (d) A34 and (f) A50. Maximum and minimum strength tests are shown.

Figure 10 shows the engineering strain – force and engineering strain – specific force curves of all three different areal weight materials at the specified directions. As in Figure 9, two representative monotonic curves are shown, corresponding to two tests of maximum and minimum tensile strength. Along the machine direction, A34 (intermediate areal weight) and A50 (highest areal weight) specimens seem to have similar peak force, which are higher than A14 (lowest areal weight). According to the engineering strain – force curves along the transverse direction, peak force increases as the areal weight of the material increases. A14 appears to have a higher peak force in the transverse direction than that in the machine direction, but its peak force is still lower than A34 and A50 along the transverse direction. Engineering strain – specific force curves demonstrate the change in force normalized by weight as a function of strain. A34 has the highest scaled strength in the machine direction whereas A14 has the highest scaled strength in the transverse direction. As a result, the monotonic tensile

behavior of specimens along the machine direction is not similar to that in the transverse direction.

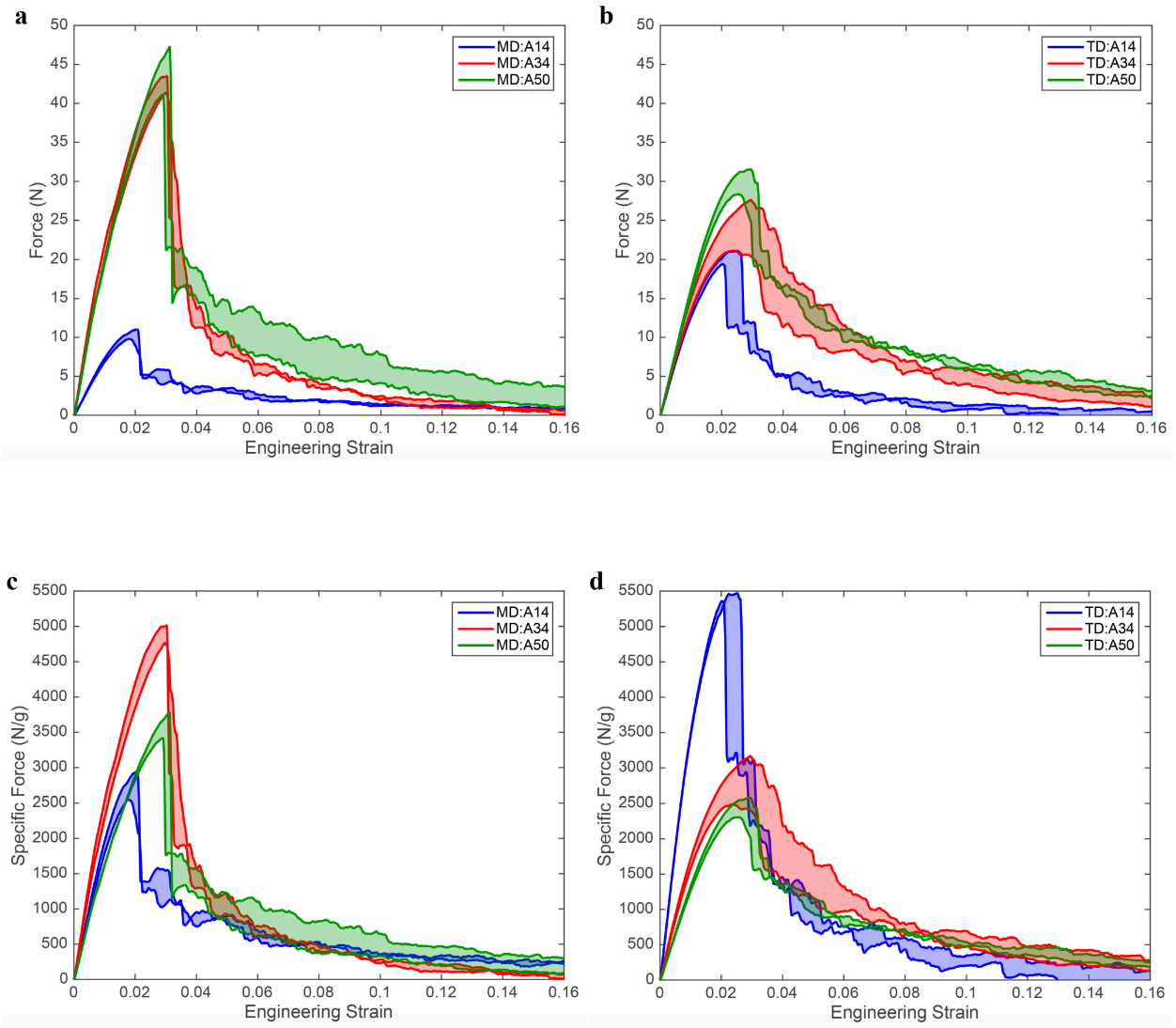

Figure 10: Monotonic tensile behavior of three types of nonwovens at a constant strain rate of 0.00588 s^{-1}. Engineering strain – force curves of all specimens in (a) machine direction (MD), (b) transverse direction (TD) and engineering strain – specific force curves of all specimens in (c) machine direction (MD), (d) transverse direction (TD)

Table 2: Mechanical properties of nonwoven specimens and constituent fiber under uniaxial tensile loading at a constant strain rate of 0.00588 s^{-1}. Mechanical properties of nonwoven specimens are shown for machine direction (MD) and transverse direction (MD).

Specimen		Young's modulus (MPa)	Scaled modulus (kN/g)	Scaled strength (kN/g)	Failure ε_f
A14					
	MD	423.91 ± 8.19	201.73 ± 4.56	2.80 ± 0.07	0.0186 ± 0.0005
	TD	734.64 ± 15.54	360.77 ± 2.94	5.48 ± 0.07	0.023 ± 0.0011
A34					
	MD	427.39 ± 22.32	252.59 ± 13.19	4.89 ± 0.12	0.0302 ± 0.0002
	TD	284.39 ± 7.35	177.42 ± 4.90	2.99 ± 0.14	0.0279 ± 0.0014
A50					
	MD	309.25 ± 3.82	172.75 ± 2.25	3.63 ± 0.07	0.0306 ± 0.0005
	TD	233.20 ± 3.07	129.80 ± 1.58	2.41 ± 0.05	0.0271 ± 0.0007
Fiber		87830 ± 1630	10158.8 ± 189	427.70 ± 11.88	0.0441 ± 0.0013

Mechanical properties of the three types of aramid nonwoven specimens both in the machine and transverse directions and constituent aramid fiber have been tabulated in Table 2. The specimen with the lowest areal weight (A14) seems to have the highest Young's modulus and the scaled modulus along the transverse direction among all of the tested samples. However, along the machine direction intermediate areal weight material (A34) appears to have the highest moduli. Contrary to expectations, A50 shows the lowest moduli both in the machine and transverse directions, although it has the highest areal weight. This unexpected correlation between areal weight and stiffness will be later explained with XRD experiments. Monotonic tensile loading shows that A14 has

the highest scaled strength along the transverse direction and A34 has the highest scaled strength along the machine direction among the three nonwovens types. A34 and A50 have later failure initiation than A14 along the machine direction and A34 has a higher failure strain than other two types of nonwovens along the transverse direction.

To investigate the relaxation behavior, nonwoven specimens and single fibers were stretched at a constant strain rate of 0.00588 s^{-1}. Specimens were suddenly deformed by a fixed amount of strain of 0.01 and were held at this strain for 10 min. Figure 11 shows the typical force – time relaxation curve of A34 specimens. Peak force (F_{peak}) was reached where the strain is 0.01 and the stable force (F_{600}) was defined as the force at 600 s. The difference between F_{peak} and F_{600} was used to calculate the amplitude change of the specimen.

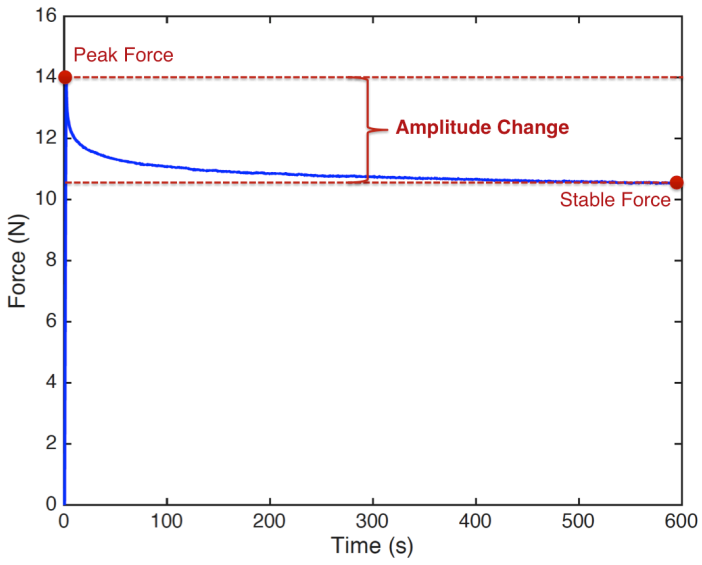

Figure 11: Typical force – time relaxation curve of A34 specimen at a strain of 0.01.

Table 3 shows the amplitude change for stress relaxation curves at constant strain rate for all nonwoven types and single fiber. Amplitude change appears to be very similar for all types of nonwoven specimens and they all have more decay in amplitude than the individual fiber.

Table 3: Amplitude change of stress relaxation curve for nonwoven specimens and single aramid fiber at a constant strain rate of 0.00588 s^{-1}.

Strain Rate s^{-1}	**0.00588**
Specimen	**Amplitude change (%)**
A14	27.30 ± 0.40
A34	27.86 ± 1.30
A50	28.07 ± 0.35
Fiber	10.43 ± 0.68

Eq. 2 describes the stress relaxation phenomenon for Maxwell model, which is the decrease in stress as a function of time under constant strain.

$$\sigma = \sigma_o \exp\left(-t/\tau\right) \qquad \text{Eq. 2}$$

The stress relaxation curve is a combination of short and long time relaxation. If there were only a short time relaxation, the curve would be completely flat after the drop. In case of solely long time relaxation, there would not be a deep drop. It is apparent that short and long time relaxation are both present in the relaxation curves. Overall, the

curves are perpetually relaxing and not approaching to a steady state. Long time relaxation constant is picking up the very slight decrease at the end when whole curve was analyzed. Combining short and long time relaxation constants is not a good practice, since the majority of data points are in the long time relaxation region and they dominate in overall time constant. Short time relaxation constant was calculated based on the time needed for the stress to decrease to 0.37 (1/e) of the initial stress[39]. Short time relaxation constant (τ) was found from calculated force as in Eq. 3 for each curve.

$$F(t) = 0.37\left(F_{peak} - F_{600}\right) + F_{600} \qquad \text{Eq. 3}$$

Table 4: Short time relaxation constant of stress relaxation curve at three different strain rates: 0.00588 s^{-1}, 0.0588 s^{-1} and 0.588 s^{-1} for nonwoven specimens.

Strain Rate (s^{-1})	**0.00588**	**0.0588**	**0.588**
Specimen	**Relaxation Time (s)**	**Relaxation Time (s)**	**Relaxation Time (s)**
A14	19.55 ± 1.03	12.43 ± 1.80	16.03 ± 0.43
A34	7.39 ± 1.72	2.20 ± 0.81	3.23 ± 0.41
A50	13.21 ± 1.45	5.63 ± 1.62	5.58 ± 1.05

Short time relaxation constants of stress relaxation curves at three different strain rates are listed in Table 4. Calculations suggest that lowest areal weight material (A14) has the longest relaxation time whereas the intermediate areal weight material (A34) has the shortest relaxation time among the three areal weights at all strain rates. Relaxation time for highest areal weight material (A50) seems to be between A14 and A34. These results are consistent with the measured mechanical properties of nonwoven

specimens, which indicate that A34 has the highest and A14 has the lowest scaled strength among the three types of nonwovens in the machine direction.

4.2. Fiber mechanical behaviors

In monotonic tensile testing, aramid fibers exhibit an essentially linear engineering strain – force and engineering strain – specific force curves as shown in Figure 12. All fibers appear to have rupture-like failure occurring around a strain of 0.04. The mechanical properties of fibers are listed in Table 2 with the nonwoven materials. The fiber modulus is approximately 50 times the scaled nonwoven modulus and the fiber scaled strength is approximately 110 times the scaled nonwoven strength.

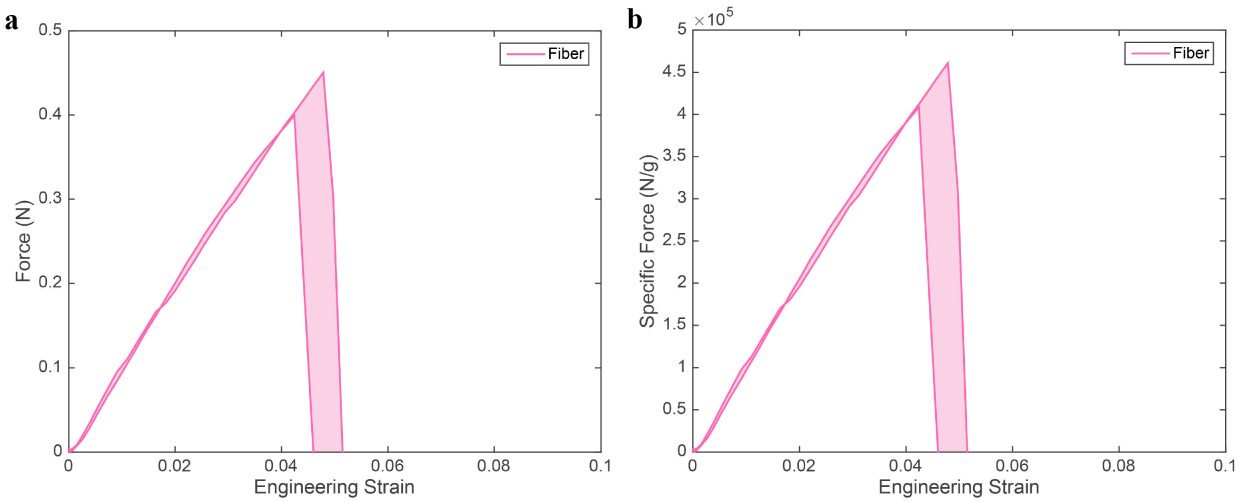

Figure 12: Monotonic tensile behaviors of single aramid fibers at a constant strain rate of 0.00588 s-1. (a) Engineering strain-force (b) Engineering strain – specific force.

During stress relaxation tests, percent change in force amplitude for the single aramid fibers is reported as 10.43 ± 0.68 in Table 3. Significant difference between the fiber and the nonwoven stress relaxation behavior has been observed. Fibers are exposed to less strain in a nonwoven than they do on their own to the same applied strain. Decay in amplitude for fibers is much smaller than amplitude change for all nonwoven specimens. Nonwoven specimens consist of staple aramid fibers and a thermoplastic binder. The difference between fiber and nonwoven relaxation amplitude change suggests that most of the nonwoven relaxation can be attributed to the binder relaxation.

4.3. FESEM

4.3.1 Undeformed nonwoven

The morphology of the fiber network was observed using FESEM. FESEM images of the nonwoven specimens that exhibit different areal weights are shown in Figure 13. Images obtained by the FESEM indicate that all of the fibers in the samples seem to be circular with clean and smooth surfaces with a cross section of approximately 12 μm as stated in the material data sheet. FESEM images also indicate qualitative information about the binder distribution. Images show that the binder is scattered in a discontinuous pattern throughout the nonwoven surface.

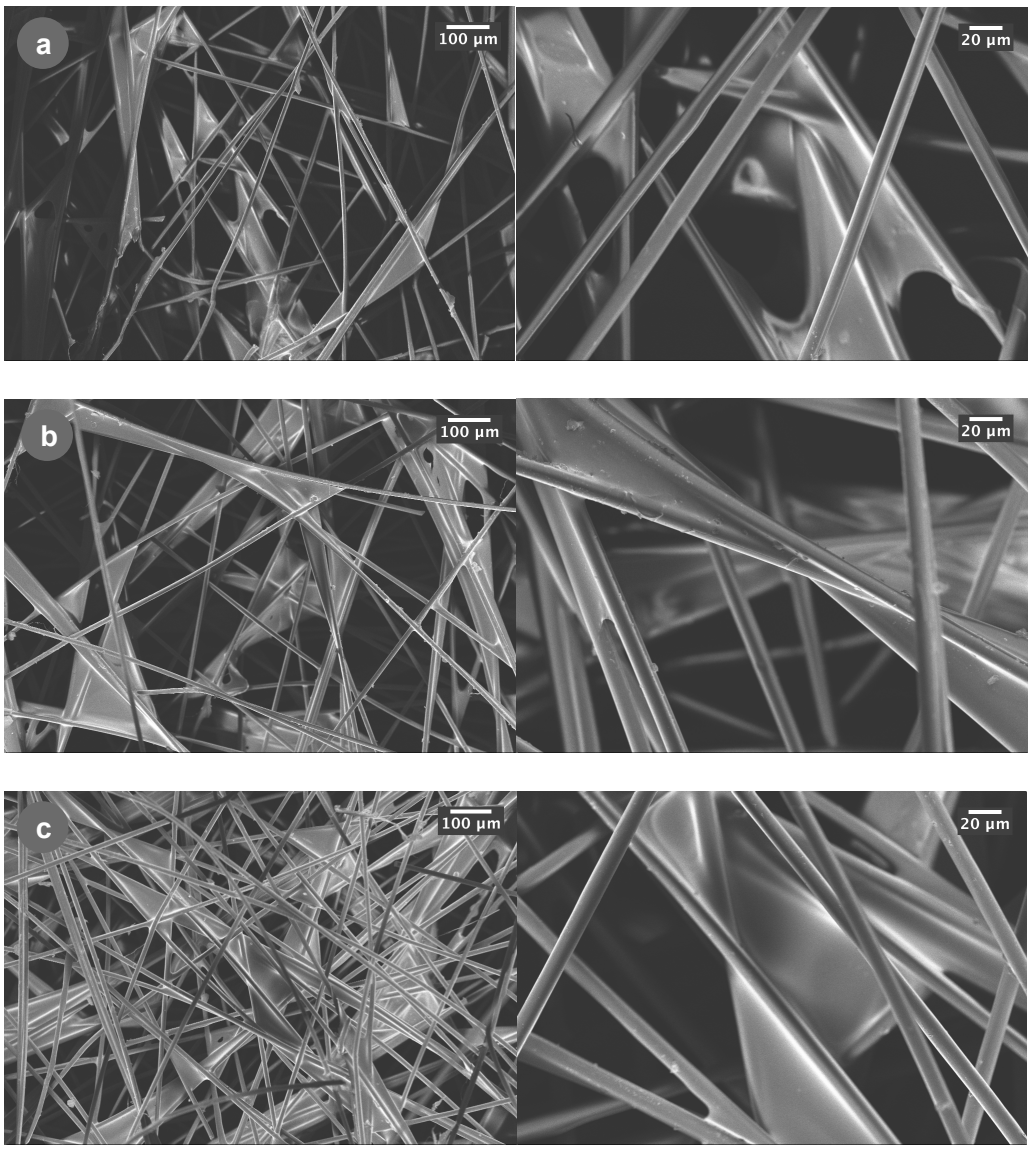

Figure 13: FESEM images of nonwoven specimens as a function of areal weight (a) A14, (b) A34, (c) A50.

4.3.2. Deformed nonwoven

As described in Section 3.1, nonwoven specimens were stretched until failure occurred. Multiple FESEM photographs as shown in Figure 14 were taken to scan the width of the specimen's fracture surface to understand the cause of the breakage. Fiber-fiber and

fiber-binder breakage are two possible mechanisms for the nonwoven deformation. Photographs demonstrate that most of the failure occurred from the fiber – binder interactions. For future work, quantitative characterization of fiber distribution needs to be studied in order to understand the deformation mechanism better.

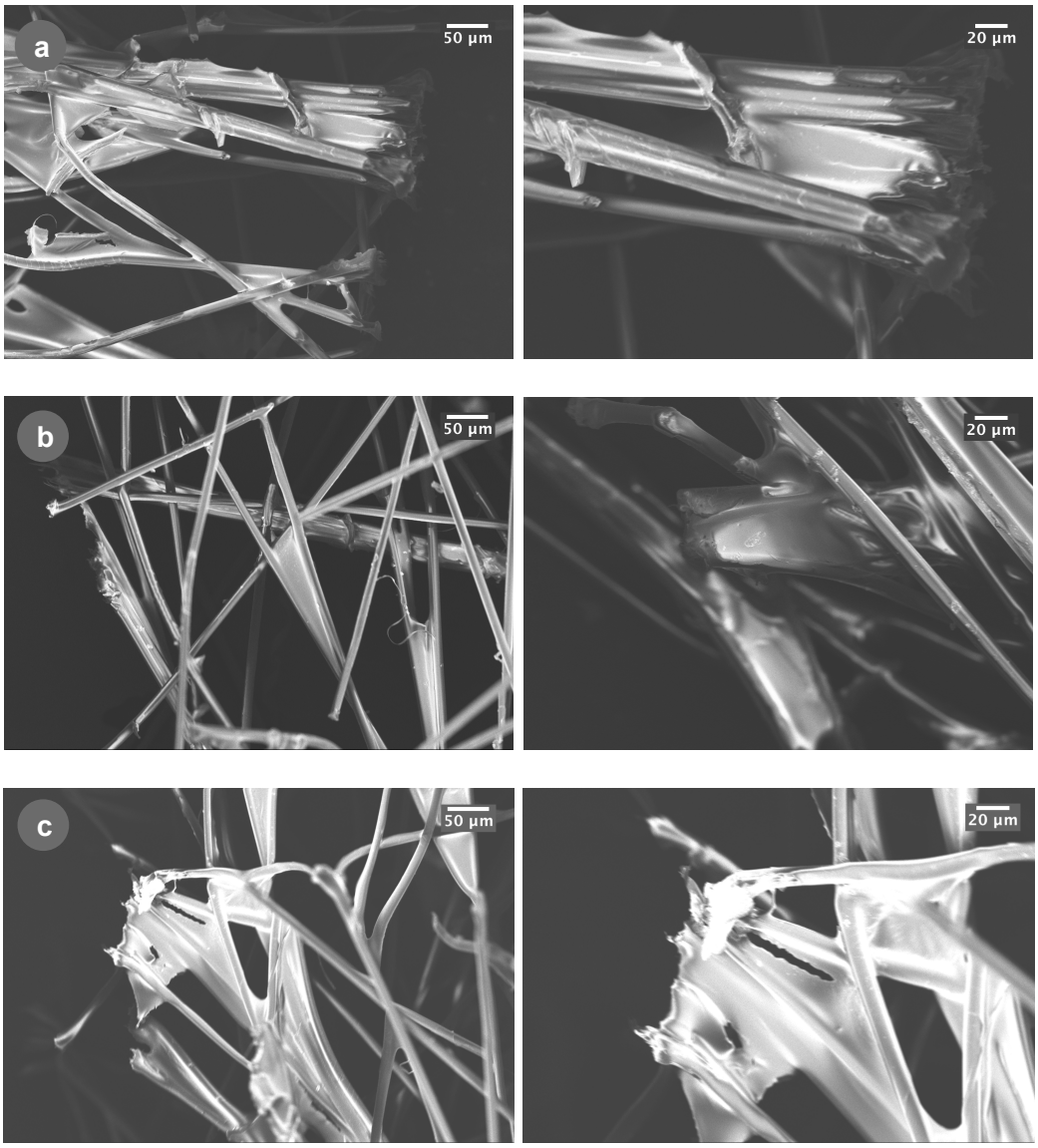

Figure 14: FESEM images of deformed nonwoven specimens as a function of areal weight (a) A14, (b) A34, (c) A50.

4.4. Micro-computed tomography

The purpose of the μCT experiment was to obtain a 3D visualization of the microstructure change under deformation in order to understand the deformation mechanisms of nonwoven specimens through the thickness. μCT images provide the microstructure change in the z direction, which cannot be obtained by FESEM imaging.

The nonwoven 3D microstructure was studied using micro computed tomography (μCT). A customized setup enabled μCT imaging during uniaxial deformation. Six different strains are picked on the monotonic loading curve of the nonwoven specimens and μCT scans were performed at each point. Figure 15 shows the 3D microstructures of the A50 specimen at six different strains. Fibers in the specimen seem to reorient during monotonic tensile loading. Before a strain of 0.025, minimal change in material microstructure can be observed. The tension force straightens the axial directional fibers and breaks their bonds with attached transverse directional fibers and binders at the beginning of the deformation. Only axial directional fibers was found to connect the two ends of the sample when significant macroscopic damage was occurred. As the specimen is stretched to a strain of 0.025, the thickness of the specimen has increased due to breakage of some interlayer bonds and some of the fibers and binder in certain parts of the specimen. Interlayer delamination was apparent as the strain increased from 0 to 0.035.

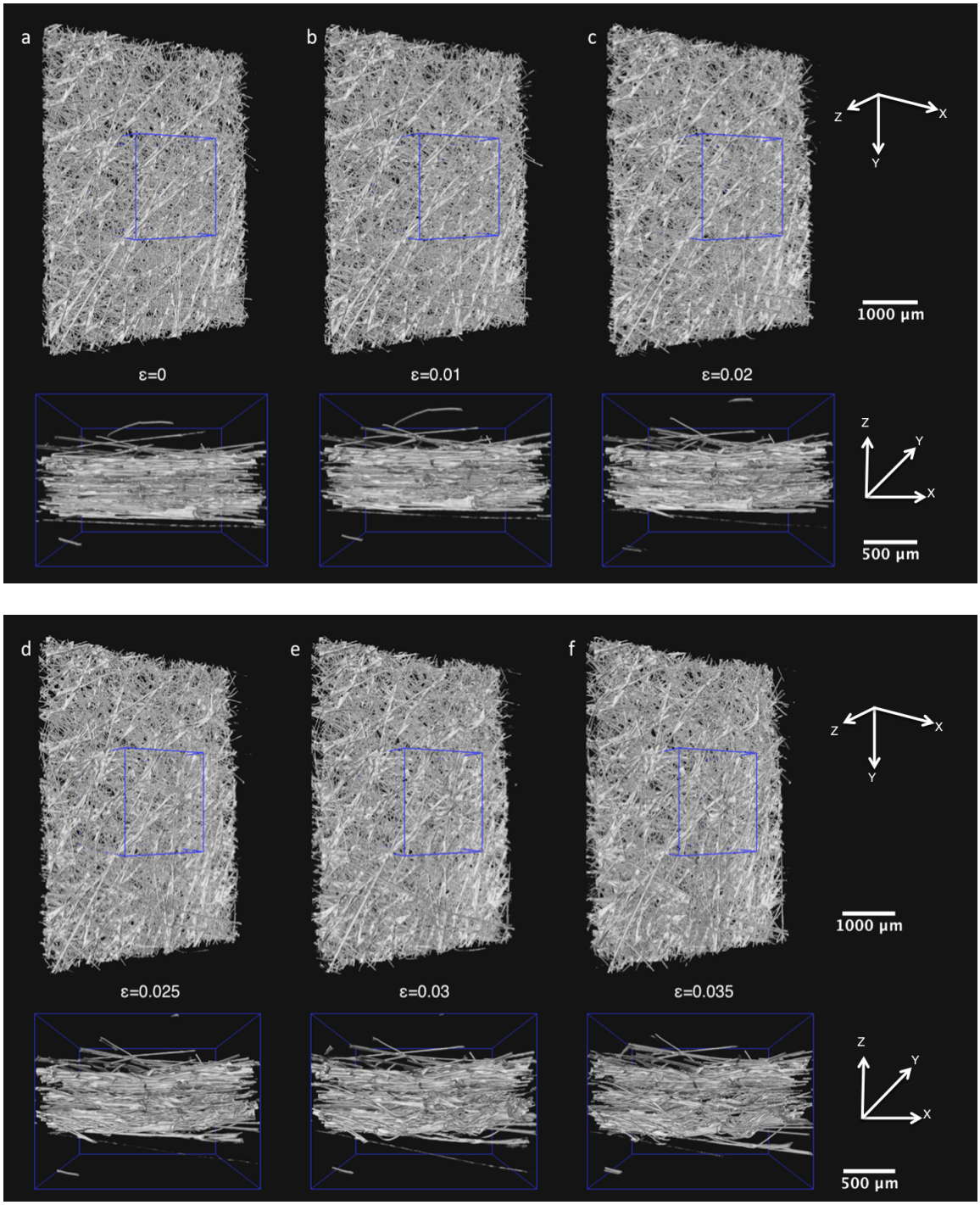

Figure 15: 3D microstructure images of a nonwoven A50 specimen at strains of (a) 0, (b) 0.01, (c) 0.02, (d) 0.025, (e) 0.03 and (f) 0.035. Top: full 4.5 mm by 4.5 mm reconstructed volume. Bottom: an enlarged partial view.

4.5. TGA analysis

TGA curves of the three different nonwoven specimens and the constituent aramid fiber are shown in Figure 16. Twaron aramid fiber is thermally stable to about 500°C. A weight loss of 3wt.% was observed before 100°C, suggesting that water is possibly removed from the fiber. Then, no further change up to 300°C could be observed and only a small weight reduction (<1wt.%) was seen within the range of 300-500°C. The thermal yield temperature was found to be around 500°C, after which the loss became progressively larger. The presented TGA results are consistent with Twaron 1000 fibers in the literature[40].

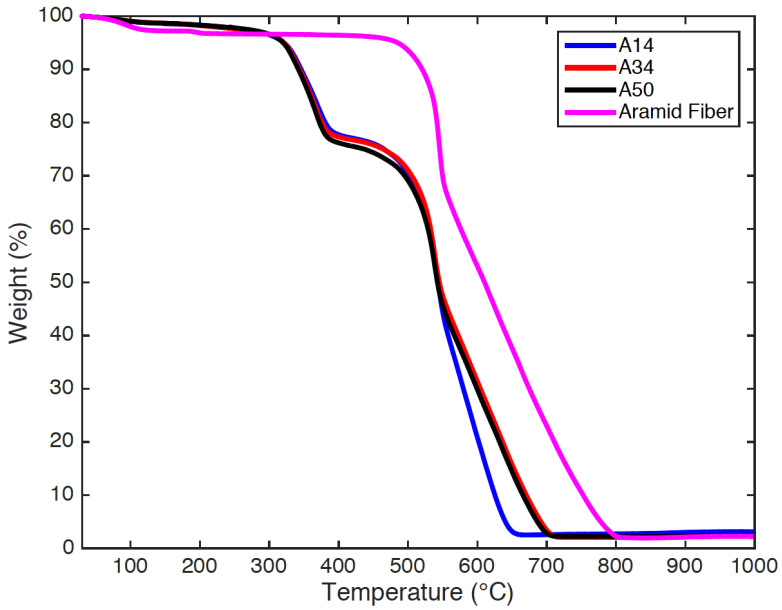

Figure 16: TGA analysis of three types of nonwoven specimens; A14, A34, A50 and aramid fibers**.**

TGA results also implies that nonwoven specimens show an initial 1.5wt.% loss of water around 100°C and a 20wt.% weight reduction near 350°C due to the melamine formaldehyde resin, which is on par with the literature[41]. The thermal yield temperature for the nonwowen specimens was also found to be near 500°C as in agreement with the aramid fibers. These results enable the determination of binder to fiber ratio in nonwoven specimens as two distinct degradation temperatures can be observed for the binder and the fiber. TGA curves of the aramid fiber and the nonwoven specimens show that approximately 20wt.% of the samples consist of the binder for all types of nonwoven specimens.

4.6. XRD analysis

Calibration was performed by using CeO_2 powder before the in-situ XRD experiments. 2θ value of CeO_2 for (111) is reported as 28.6° for 8 keV of beam energy (λ=1.5418Å) in the literature[42]. The beam energy was set to 10 keV in the XRD experiments. Wavelength of the incident beam (λ) used in the XRD experiments at CHESS is calculated as shown below for 10 keV of beam energy:

$$\mathrm{E(eV)} = \frac{\mathrm{hc\ (eV)}}{\lambda\ (\mu\mathrm{m})} \Longrightarrow\ \lambda = \frac{1.2398}{10000} = 0.00012398\mu\mathrm{m} = 1.2398\text{Å}$$

where E is the beam energy, h is the Planck constant, and c is the speed of light. 2θ value of CeO_2 can be calculated as:

$$\lambda = 2dsin\theta \Longrightarrow sin\theta = \frac{\lambda}{2d} = \frac{1.2398}{2 * 3.125} = 0.198368 \Longrightarrow \theta = 11.44° \; and \; 2\theta = 22.9°$$

where d is the distance between atomic layers in a crystal (d=3.125Å for CeO_2), and θ is the diffraction angle. Difference in reported 2θ angles is expected due to the difference in the beam energy used in both of the experiments.

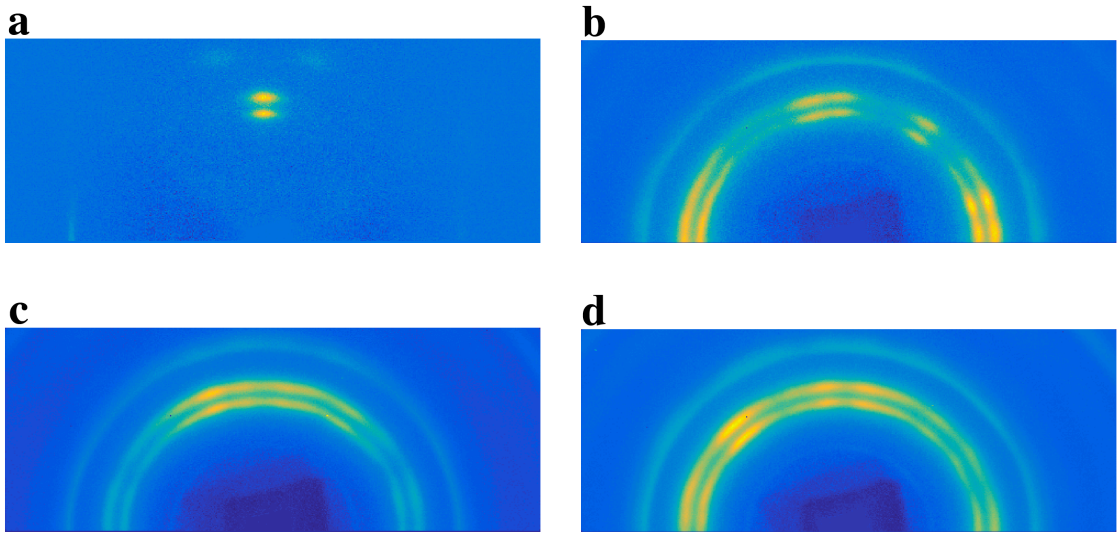

Figure 17: 2D XRD pattern of (a) a single aramid fiber, an undeformed aramid nonwoven specimens (b) A14, (c) A34, (d) A50.

Figure 17 a displays the XRD pattern of a single horizontally aligned fiber. The fiber is placed parallel to the loading axis. From the fiber XRD pattern two distinct diffraction peaks are observed at a diffraction angle (2θ) of 16.2° and 18.3° corresponding to the crystalline planes aligned in (110) and (200) directions, respectively. This diffraction pattern is consistent with Twaron aramid fibers[43] and Kevlar fibers[44,45] considering different wavelengths (λ=1.5418Å with 8 keV beam energy) are used in both of the experiments. Aramid fiber is highly anisotropic, thus high Young's modulus and tensile

strength are observed only in one direction. Weak hydrogen bonds in the transverse direction cause poor transverse properties[46].

The diffraction patterns of undeformed A14, A34 and A50 nonwoven specimens are shown in Figure 17 b, c, d. The equatorial scan gives two sharp diffraction peaks, one at 2θ of 16.2° for the (110) plane and one at 18.3° for the (200) plane. A minor peak often appears at 24.5° for the (211) plane. XRD pattern of A14 indicates that most of the fibers are initially aligned in the transverse direction and a few of the fibers are aligned in the loading direction, which is also the machine direction of the specimens. On the other hand, according to the XRD pattern of A34 specimens, the majority of the fibers are aligned in the machine direction. A50 specimens seem to have the majority of the fibers aligned between the machine and the transverse directions. According to the 2D XRD patterns of nonwoven specimens, it can be concluded that the initial fiber orientation alignment is significantly different for all types of nonwovens. These XRD patterns give insight to clarify the uncorrelated mechanical properties of nonwoven specimens as a function of areal weight. A14 has the highest strength and moduli when tested along the transverse direction and A34 has the highest strength and moduli when tested along the machine direction. Majority of the fibers are originally aligned in the transverse and machine directions for A14 and A34, respectively. A50 has the lowest moduli both in the machine and the transverse directions because of its initial fiber orientation distribution. It is possible to get lower moduli both in the machine and transverse directions by having an off axis fiber alignment.

4.7. Fiber orientation evolution under uniaxial tensile testing

Fiber orientation distribution needs to be investigated to understand the nonwoven deformation. XRD experiments were performed in order to analyze the effect of areal weight on the fiber alignment. The aramid fibers present in the nonwoven specimens consist of fully extended polymer chains formed along the fiber axis with a high degree of crystallinity, which makes XRD a suitable method to analyze fiber orientation distribution.

Figure 18 shows the fiber orientation distribution functions at five representative strains for all nonwoven types and each type of fiber orientation parameter of nonwoven as a function of engineering strain during uniaxial tensile test. The fiber orientation distribution functions of A14, A34 and A50 specimens at five different strains are shown in Figure 18 a, c, e, respectively. For A14 specimens, the peaks of the fiber orientation distribution are around 10° and 170°, inferring that majority of the fibers are aligned perpendicular to the loading axis. The fibers align between 120° and 160° as the strain increases from 0 to 0.04. For A34 specimens the peak of the fiber orientation distribution is between 80° and 120°, indicating that most of the fibers are initially aligned with the loading axis under uniaxial tensile loading. The peak height increases gradually as the strain increases from 0.01 to 0.04. For A50 specimens, the peak height at 0 strain appears between 100° and 120°. Also the peak height moves approximately to 100° at 0.04 strain. The change in the peak height for A50 is less than for A34, which

indicates that the reorientation process in A50 specimens was less significant than in A34 specimens.

The orientation parameter p (Eq. 1) as a function of engineering strain is shown in Figure 18 b, d, f. The orientation parameter values at 0 strain for all specimens are consistent with the 2D XRD patterns of undeformed nonwovens. According to the data analysis, A14 specimens have the lowest and A34 specimens have the highest p value. A50 specimens remain between A14 and A34 in terms of p value. The orientation parameters of A14, A34 and A50 have an overall trend of increase in parameter p as the strain increases, which suggest that fibers became more aligned in the direction of the loading axis as the deformation occurs.

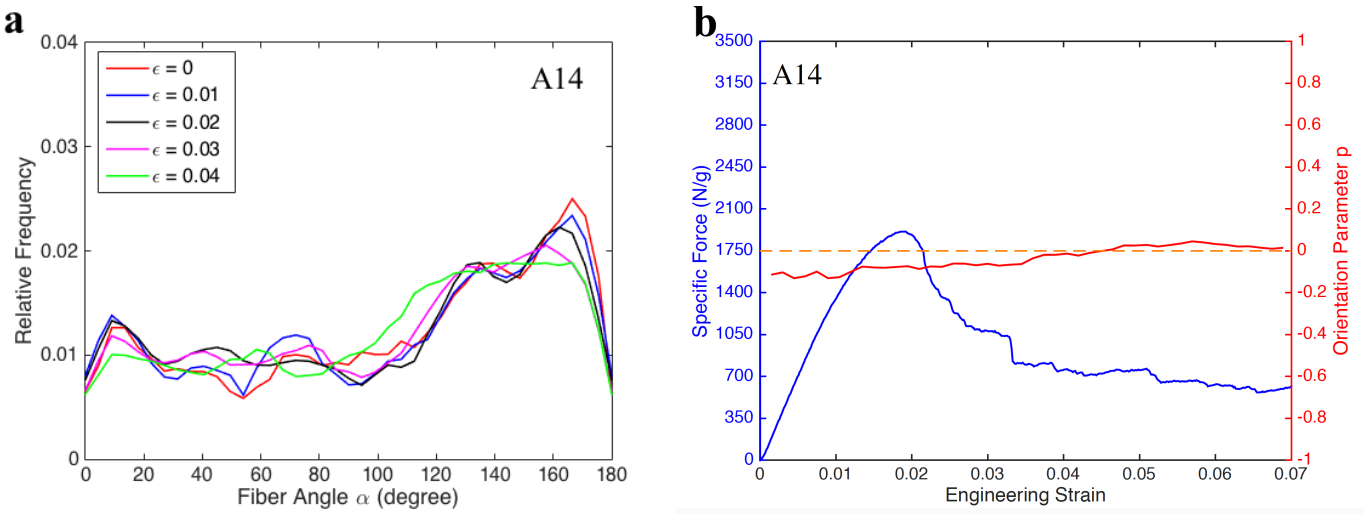

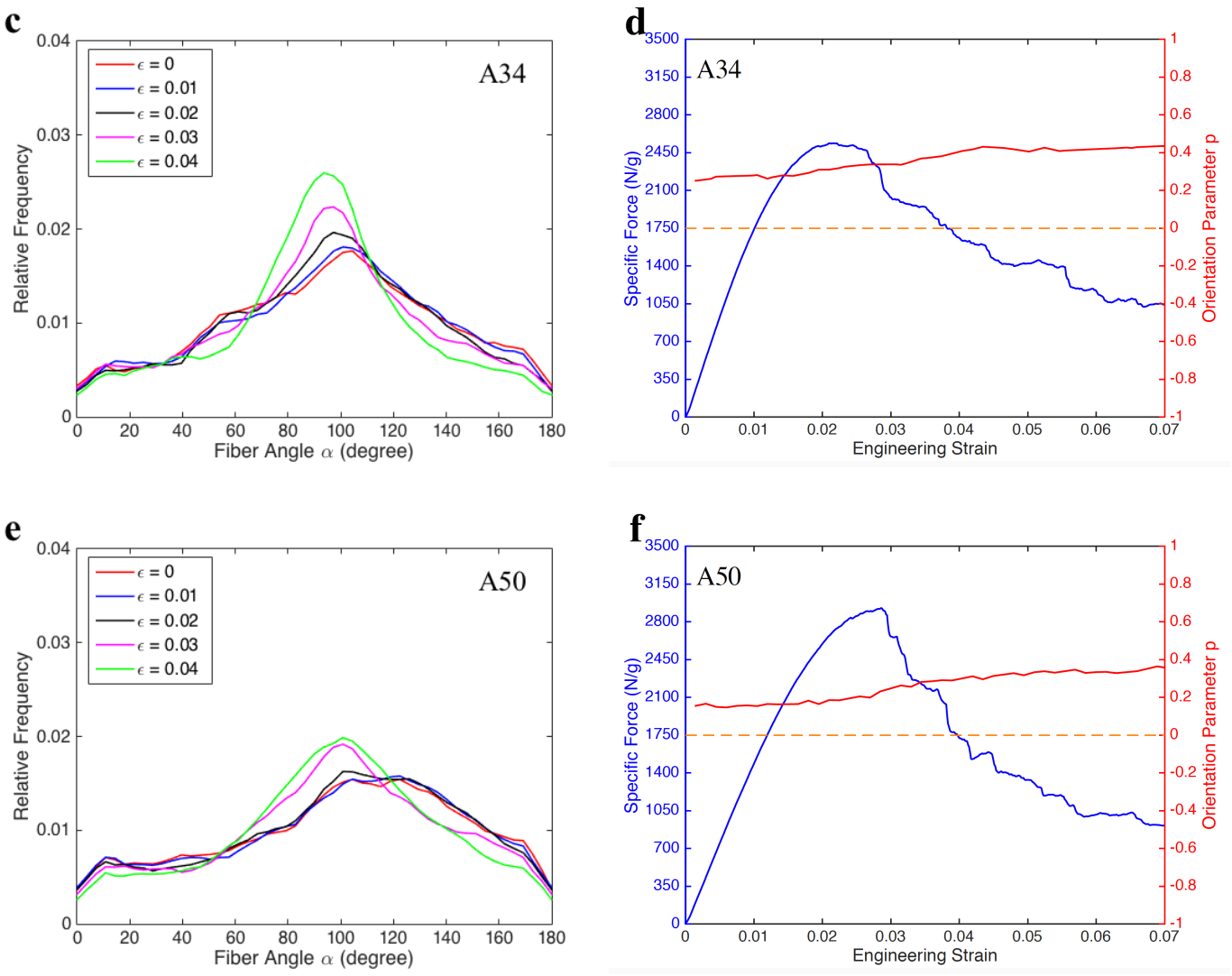

Figure 18: Fiber orientation change extracted from XRD patterns taken during monotonic tensile loading at a strain rate of 0.00147 s^{-1}. The full fiber orientation distributions of (a) A14, (c) A34 and (e) A50 at 5 different strains. Specific force and orientation parameter as a function of engineering strain for (b) A14, (d) A34 and (f) A50.

4.8. Fiber orientation evolution under relaxation tests

The fiber orientation distribution curves taken during stress relaxation tests are shown in Figure 19. Fiber orientation distributions at four different time points: the initial point, the

onset point of relaxation, 50 s and 100 s after relaxation are plotted for each type of nonwoven type. Initial represents the beginning of the experiment where time is 0. Relax for 0s is the point where the peak force is reached at 0.01 strain. Relax for 50s and 100s indicate the time passed after the strain is 0.01.

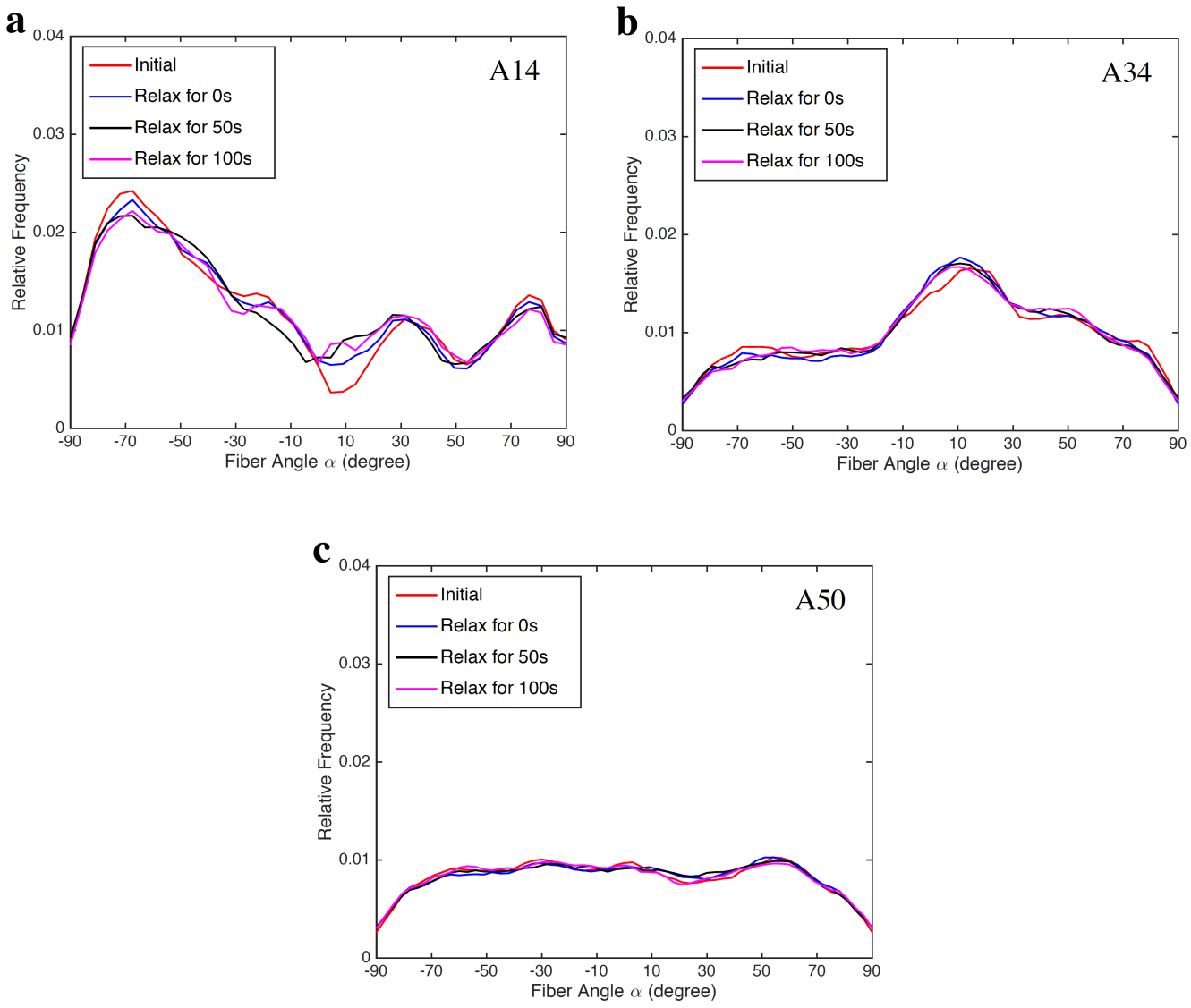

Figure 19: Fiber orientation change extracted from XRD patterns taken during stress relaxation test at a strain rate of 0.00147 s^{-1}. The full fiber orientation distributions of (a) A14, (b) A34 and (c) A50.

The number of fibers aligned in -70° and 10° change significantly during the first 100 s of relaxation for the A14 specimen. For the A34 specimen, the number of fibers aligned in 10° increases slightly during the onset point of the relaxation. Minimal, almost negligible fiber orientation change within 100 s of relaxation time is observed for the A50 specimens. The XRD results indicate that the nonwoven microstructure is not changing during the relaxation tests and the macroscopic stress relaxation is mainly caused from binder relaxation rather than the structure change.

CHAPTER 5

CONCLUSION

5.1. Summary

In this work, the deformation mechanisms of aramid nonwoven specimens and the relationship between these mechanisms and their areal weights were investigated. Macroscopic mechanical behavior of nonwoven specimens and single aramid fibers were studied using monotonic tensile and stress relaxation tests. FESEM, TGA, and in-situ μCT experiments were carried out to understand the microstructure of these nonwoven specimens. Then, fiber orientation evolution of nonwoven specimens under deformation was studied using in-situ XRD experiments.

Engineering strain – specific force curves indicated the “elastic-plastic” behavior of the nonwoven specimens with a rupture-like failure mode. All nonwoven types regardless of their areal weight were prone to fail in rupture-like manner. Furthermore, intermediate areal weight nonwoven specimens (A34) prepared in the machine direction exhibited higher modulus, scaled modulus, and scaled strength among the three types of nonwovens. On the other hand, low areal weight nonwoven specimens (A14) prepared in the transverse direction showed higher modulus, scaled modulus and scaled strength among the three types of nonwovens. These findings on the mechanical properties were supported by the studies conducted on the initial fiber orientation alignment of the

nonwovens obtained from 2D XRD patterns. According to the XRD patterns of the nonwovens, most fibers were already aligned in the transverse and machine directions for A14 and A34, respectively. XRD pattern of higher areal weight nonwoven specimens (A50) indicated that the majority of the fibers fall between the machine and the transverse directions. Therefore, A50 specimens showed the lowest moduli both in the machine and the transverse direction due to the off axis fiber alignment. Mechanical characterization of constituent aramid fibers revealed that the fiber was also elastic-plastic with its stiffness close to fifty times to the scaled nonwoven stiffness. Moreover, in the stress relaxation experiments, stress decreased for all types of nonwoven specimens, and the decay in the magnitude was similar for all types. The fiber relaxation itself was smaller than the nonwoven relaxation, thus the difference between two caused by the binder relaxation.

FESEM and in-situ μCT experiments were used to visualize the deformation mechanism of nonwoven specimens. According to the FESEM images, most of the fiber breakage at the fracture surface occurred where the fiber – binder interaction was present. μCT scans suggested that interlayer delamination became visually apparent as applied strain increased. Nonwoven fiber orientation evolution during tensile loading and relaxation tests was investigated by using in-situ XRD experiments. The orientation parameter of all types of nonwoven specimens showed an overall trend of increase in the parameter p as the applied strain increased. A14 specimens had majority of the fibers aligned in the transverse direction resulting in a negative p value and A34 specimens had most of

the fibers aligned in the machine direction resulting in a positive p value. Orientation parameter of A50 specimens was calculated between A14 and A34 specimens. In the stress relaxation experiments, almost negligible fiber orientation change occurred for A34 and A50 specimens. On the other hand, fiber orientation change was observed for A14 specimens suggesting that majority of the fiber orientation occurred before the onset point of relaxation.

This study indicates that areal weight is not necessarily a predictor of the scaled mechanical properties, and initial fiber orientation of the nonwoven specimens plays a vital role in the mechanical performance of these materials. Better macroscopic mechanical properties such as highest scaled strength and moduli are not obtained from the highest areal weight nonwoven specimens, however obtained from the specimens, in which the majority of the fibers were aligned in the testing direction. Therefore, the initial fiber orientation is an important parameter to consider the macroscopic mechanical behavior of nonwoven specimens. Although the experiments were conducted with nonwoven specimens consists of staple aramid fibers, correlation between initial fiber orientation and macroscopic mechanical properties are expected for other nonwoven materials due to inherent similarities in the evolution of fiber network upon mechanical properties.

5.2. Future work

The primary direction for future work to better understand the relationship between the microstructure and the mechanical behavior of aramid nonwoven specimens is to identify the effect of the binder on the deformation mechanisms. Even though the qualitative binder distribution in aramid nonwoven specimens was investigated by FESEM images, quantitative spatial distribution of binder should be studied before any conclusion about the effect of binder on the mechanical properties can be drawn. In order to accomplish this, nano-CT scans can be used to image the initial nonwoven microstructure. Additionally, nonwoven deformation micromechanisms can be visualized at increasing levels of strains by using μCT scans. Due to confidentiality on the composition of the tested samples, no information was obtained for the type of binder utilized in the samples. After obtaining this information, further mechanical testing on the binder material should be conducted to better understand the contribution of the binder to the mechanical strength. Combining individual mechanical responses of the binder and the fiber coupled with a comprehensive microstructural data set should be sufficient to build a microstructure-based constitutive model in future work.

APPENDIX

A.1 Developed Programs

The MATLAB code used in this thesis was revised from the code used in our recent publication[6]. A brief description of the developed programs for performing the work presented in this thesis are given in the table below:

Program	**Description/Usage/Related Programs**
main_frame.m	Code to generate parameter matrix for a single XRD frame. Parameter matrix includes maximum intensities (A1, A2), full widths at half max (w1, w2), and distances from center of the peak (x0, x00).
cut_span.m	Code to divide each XRD frame into specified number of slices starting from 0° to 180°. *Related program:* main_frame.m
integrate.m	Code to display each slice within the XRD frame, then to integrate each slice and to obtain associated 2theta – intensity graph for each slice. *Related program:* main_frame.m
fitting.m	Code to fit the experimental data to the fitting function in 2theta – intensity graph for each slice. *Related program:* main_frame.m
fun.m	Code to specify the fitting function. *Related program:* fitting.m

main_frame.m

```
% This program is used to generate parameter matrix for a single XRD frame
% Note the difference between frame and slice. A frame can be cutted into slices.

clc;
clear;
close all;
```

```
%%
%% Experimental setup input
% pxs: pixel size; dist: sample detector distance [mm];
% Beam center -> cm: the row number; cn: the column number;
pxs = 172;
dist = 73.414;
cm = 195;
cn = 236;

%%
%% Pre-processing
% Read the first XRD image and beam profile image

dir1 = ['/Users/simgeuzun/Desktop/XRD_Data/Stress Relaxation Data/S50-9/'];
dir2 = ['/Users/simgeuzun/Desktop/XRD_Data/Stress Relaxation Data/Beam Profile50-
9/'];

img_name = strcat(dir1,'S50-9_series__0090','.tiff');
BP_name = strcat(dir2,'BeamProfile50-10__0090','.tiff');

img = imread(img_name,'tiff');
BP = imread(BP_name,'tiff');
figure(1);
imagesc(img-BP);

% Get rid of the deadband
[rind,~]=find(BP==-1);
bandedrows=min(rind):size(BP,1);
BP(bandedrows,:)=[];
img(bandedrows,:)=[];

% Substract the beam profile image from the XRD image
img3 =img-BP;
figure(1);
imagesc(img3);
axis equal;

%%
% Choose the baseline and region of interest
% Need to modify if needed
x1 = [0;1];
y1 = [0;0];
% x2 is the 2theta region that you would like to analyze
```

```
x2 = [120,146];
%%
%% Generate fitting parameters of each slice in each frame
% numsl = number of slices that each frame is divided into
% phi = angle of each slice in one direction; phix2 is the angle of the pie
numsl = 50;
phi = 5;

% Initialize the parameter matrix
% (number of slices * 6 parameters * number of frames)
% Loop through all the slices
xrdsl = cut_span(img3,cm,cn,numsl,phi);
for slnum =1:numsl
    % reads from center to 2theta, not region of interest
    xrdxy = integrate(xrdsl(:,:,slnum),cm,cn,pxs,dist);
    xrdprm50_e01(slnum,:)=fitting(xrdxy,x1,y1,x2);
end

figure()
plot(xrdprm50_e01(:,1),'-r')
```

cut_span.m

```
function output = cut_span(image,cm,cn,num,phi)

[m,n] = size(image);

%Initialize output
output = zeros(m,n,num);

%Loop over all the slices
for i = 1:num
    theta = (180/num)*(i-1);
    mark1 = cosd(theta+phi);
    mark2 = cosd(theta-phi);

    %The slice is close to the x axis
    if mark1>0 && mark2>0 && theta<phi
        %Loop over all the pixels
        for p = 1:m
            for q = 1:n
                mark3 = atand((cm-p)/(q-cn));
                if mark3>(theta-phi) && mark3<(theta+phi) && (q-cn)>0
                    output(p,q,i)=image(p,q);
```

```
        end
      end
    end

%The slice is in the first quadrant
elseif mark1>0 && mark2>0 && theta>phi
    %Loop over all the pixels
    for p = 1:m
      for q = 1:n
        mark3 = (q-cn)/sqrt((q-cn)^2+(cm-p)^2);
        if mark3<mark2 && mark3>mark1 && (cm-p)>0
          output(p,q,i)=image(p,q);
        end
      end
    end

%The slice is close to the y axis
elseif mark1<0 && mark2>0
    %Loop over all the pixels
    for p = 1:m
      for q = 1:n
        mark3 = (q-cn)/sqrt((q-cn)^2+(cm-p)^2);
        if mark3<mark2 && mark3>=0 && (cm-p)>0
          output(p,q,i)=image(p,q);
        elseif mark3>mark1 && mark3<0 && (cm-p)>0
          output(p,q,i)=image(p,q);
        end
      end
    end

%The slice is in the second quadrant
elseif mark1<0 && mark2<0 && (theta+phi)<180
    %Loop over all the pixels
    for p = 1:m
      for q = 1:n
        mark3 = (q-cn)/sqrt((q-cn)^2+(cm-p)^2);
        if mark3>mark1 && mark3<mark2 && (cm-p)>0
          output(p,q,i)=image(p,q);
        end
      end
    end

%The slice is close to the -x axis
elseif mark1<0 && mark2<0 && (theta+phi)>180
```

```
      %Loop over all the pixels
       for p = 1:m
          for q = 1:n
             mark3 = 180-atand((cm-p)/(cn-q));
             if mark3>(theta-phi) && (cn-q)>0 && (cm-p)>0
                output(p,q,i)=image(p,q);
             elseif mark3<(theta+phi) && (cn-q)>0 && (cm-p)<0
                output(p,q,i)=image(p,q);
             end
          end
       end

   end
end

end
```

integrate.m

```
function output = integrate(image,cm,cn,pxs,dist)

[m,n]=size(image);

% Calculate the 2 theta value
% d: radius matrix;
d = zeros(m,n);

for i = 1:m
   for j = 1:n
      d(i,j) = round(sqrt((i-cm)^2+(j-cn)^2));
   end
end

dmax = max(max(d));
dmin = min(min(d));

%Integrate
intensity = zeros(dmax-dmin,1);

for r = 1:dmax
   for p = 1:m
      for q = 1:n
         if d(p,q) == r
```

```
            intensity(r)=intensity(r)+image(p,q);

        end
    end
end

end

output = zeros(dmax,2);
for t =1:dmax
    output(t,1)=atan(t*pxs/dist/1000)*180/pi();
    output(t,2)=intensity(t);
end

figure()
imagesc(image);
axis equal;

figure()
plot(output(:,1),output(:,2),'-b', 'Linewidth',2);
xlabel('Two theta','FontSize', 16);
ylabel('Intensity','FontSize', 16);
set(gcf,'Color',[1,1,1]) % background color of the figure is set to white
set(gca,'FontSize',14);
grid off
xlim([10,24]);

end
```

fitting.m

```
function [lzprm,MSE]=fitting(input,xsub,ysub,xlim)

qlin = input(:,1);
dat = input(:,2);

%Subtract the subline
datsub=ysub(1)+(ysub(2)-ysub(1)).*qlin./(xsub(2)-xsub(1));
dat2=dat-datsub;

%Use the selected region of interest
qlin3=qlin(floor(xlim(1)):ceil(xlim(2)));
dat3=dat2(floor(xlim(1)):ceil(xlim(2)));
```

```
%Fitting
x=qlin3;
yOrig=dat3;

figure()
plot(x,yOrig,'ob');
hold on;

options=optimset('Display','iter','GradObj','on','DerivativeCheck','off');
[peaks,loc,width,prominence]=findpeaks(yOrig,x);
[~,ind]=sort(prominence,'descend');

vStart=[peaks(ind(1)),width(ind(1)),loc(ind(1)),peaks(ind(2)),width(ind(2)),loc(ind(2))];
yStart=fun(vStart,x);

options=statset('MaxIter',1000,'Display','iter','Robust','off');
[lzprm,R,J,CovB,MSE]=nlinfit(x,yOrig,@fun,vStart,options);
[~,ind]=sort(lzprm([3,6]));
tmp=[lzprm((ind(1)-1)*3+1:(ind(1)-1)*3+3),lzprm((ind(2)-1)*3+1:(ind(2)-1)*3+3)];
lzprm=tmp; yStart

yEnd=fun(lzprm,x);

plot(x,yEnd,'-r','Linewidth',2);
xlabel('Two theta','FontSize', 16);
ylabel('Intensity','FontSize', 16);
legend('Data','Fit','End','Location','southeast');
%set(gca,'Color',[0.7,0.7,0.7]);
set(gcf,'Color',[1,1,1]) % background color of the figure is set to white
set(gca,'FontSize',14);

end
```

fun.m

```
function [y]=fun(v,x)
A1=v(1);
w1=v(2);
x0=v(3);
A2=v(4);
w2=v(5);
x00=v(6);

y=(A1./(1+((x-x0)./w1).^2))+(A2./(1+((x-x00)./w2).^2))
```

REFERENCES

1 Russell, S. J. *Handbook of nonwovens*. (Woodhead Publishing, 2006).

2 Picu, R. C. Mechanics of random fiber networks-a review. *Soft Matter* **7**, 6768-6785, doi:10.1039/C1SM05022B (2011).

3 Silberstein, M. N., Pai, C.-L., Rutledge, G. C. & Boyce, M. C. Elastic–plastic behavior of non-woven fibrous mats. *Journal of the Mechanics and Physics of Solids* **60**, 295-318, doi:http://dx.doi.org/10.1016/j.jmps.2011.10.007 (2012).

4 Raina, A. & Linder, C. A homogenization approach for nonwoven materials based on fiber undulations and reorientation. *Journal of the Mechanics and Physics of Solids* **65**, 12-34, doi:http://dx.doi.org/10.1016/j.jmps.2013.12.011 (2014).

5 Martínez-Hergueta, F., Ridruejo, A., González, C. & Llorca, J. Deformation and energy dissipation mechanisms of needle-punched nonwoven fabrics: A multiscale experimental analysis. *International Journal of Solids and Structures* **64–65**, 120-131, doi:http://dx.doi.org/10.1016/j.ijsolstr.2015.03.018 (2015).

6 Chen, N., Koker, M. K. A., Uzun, S. & Silberstein, M. N. In-situ X-ray study of the deformation mechanisms of non-woven polypropylene. *International Journal of Solids and Structures*, doi:http://dx.doi.org/10.1016/j.ijsolstr.2016.07.028.

7 Isaksson, P., Dumont, P. J. J. & Rolland du Roscoat, S. Crack growth in planar elastic fiber materials. *International Journal of Solids and Structures* **49**, 1900-1907, doi:http://dx.doi.org/10.1016/j.ijsolstr.2012.03.037 (2012).

8 Jeon, S.-Y. *et al.* In situ monitoring of structural changes in nonwoven mats under tensile loading using X-ray computer tomography. *Composites Part A: Applied Science and Manufacturing* **63**, 1-9, doi:http://dx.doi.org/10.1016/j.compositesa.2014.03.019 (2014).

9 Demirci, E., Acar, M., Pourdeyhimi, B. & Silberschmidt, V. V. Finite element modelling of thermally bonded bicomponent fibre nonwovens: Tensile behaviour. *Computational Materials Science* **50**, 1286-1291, doi:http://dx.doi.org/10.1016/j.commatsci.2010.02.039 (2011).

10 Chiao, C. C. & Chiao, T. T. in *Handbook of Composites* (ed George Lubin) 272-317 (Springer US, 1982).

11 Vollbracht, L. & Veerman, T. J. (Google Patents, 1981).

12 Yang, H. H. *Aramid fibers*. 199-229 (Pergamon, 2000).

13 Blades, H. (Google Patents, 1973).

14 Ahmed, D. *et al.* Microstructural developments of poly (p-phenylene terephthalamide) fibers during heat treatment process: a review. *Materials Research* **17**, 1180-1200 (2014).

15 Yang, H. H. *Kevlar aramid fiber*. (John Wiley & Sons, 1993).

16 Yang, H. H., Allen, S. R. in *Advanced Fiber Spinning Technology* 142 (Elsevier Science, 1994).

17 Yang, H. H. *Aromatic high-strength fibers.*, (Wiley, 1989).

18 Yang, H. H. (Google Patents, 1982).

19 Kumar, S. & Gupta, V. B. in *Manufactured Fibre Technology* (eds V. B. Gupta & V. K. Kothari) 514-559 (Springer Netherlands, 1997).
20 Kwolek, S. L., Morgan, P. W., Schaefgen, J. R. & Gulrich, L. W. Synthesis, Anisotropic Solutions, and Fibers of Poly(1,4-benzamide). *Macromolecules* **10**, 1390-1396, doi:10.1021/ma60060a041 (1977).
21 Morgan, P. W. Synthesis and Properties of Aromatic and Extended Chain Polyamides. *Macromolecules* **10**, 1381-1390, doi:10.1021/ma60060a040 (1977).
22 Bair, T. I., Morgan, P. W. & Killian, F. L. Poly(1,4-phenyleneterephthalamides). Polymerization and Novel Liquid-Crystalline Solutions. *Macromolecules* **10**, 1396-1400, doi:10.1021/ma60060a042 (1977).
23 Dobb, M. G. & McIntyre, J. E. in *Liquid Crystal Polymers II/III* (ed N. A. Platé) 61-98 (Springer Berlin Heidelberg, 1984).
24 Northolt, M. G. X-ray diffraction study of poly(p-phenylene terephthalamide) fibres. *European Polymer Journal* **10**, 799-804, doi:http://dx.doi.org/10.1016/0014-3057(74)90131-1 (1974).
25 Northolt, M. G. & van Aartsen, J. J. Chain orientation distribution and elastic properties of poly (p-phenylene terephthalamide), a “rigid rod” polymer. *Journal of Polymer Science: Polymer Symposia* **58**, 283-296, doi:10.1002/polc.5070580120 (1977).
26 Shim, V. P. W., Lim, C. T. & Foo, K. J. Dynamic mechanical properties of fabric armour. *International Journal of Impact Engineering* **25**, 1-15, doi:http://dx.doi.org/10.1016/S0734-743X(00)00038-5 (2001).
27 Hindeleh, A. M., Halim, N. A. & Ziq, K. A. Solid-state morphology and mechanical properties of Kevlar 29 fiber. *Journal of Macromolecular Science, Part B* **23**, 289-309, doi:10.1080/00222348408219461 (1984).
28 Frank, F. C. The Strength and Stiffness of Polymers. *Proceedings of the Royal Society of London. A. Mathematical and Physical Sciences* **319**, 127-136, doi:10.1098/rspa.1970.0170 (1970).
29 Heinrich, K. & Jung, H. New Concepts in para-Aramid Fibers. *Textile Research Journal* **62**, 771-775, doi:10.1177/004051759206201210 (1992).
30 Ozawa, S. A New Approach to High Modulus, High Tenacity Fibers. *Polym J* **19**, 119-125, doi:10.1295/polymj.19.119 (1987).
31 Bourbigot, S., Flambard, X. & Poutch, F. Study of the thermal degradation of high performance fibres—application to polybenzazole and p-aramid fibres. *Polymer Degradation and Stability* **74**, 283-290, doi:http://dx.doi.org/10.1016/S0141-3910(01)00159-8 (2001).
32 Chapman, R. *Applications of nonwovens in technical textiles*. (Elsevier, 2010).
33 <http://www.edana.org/discover-nonwovens/how-they're-made/formation> (
34 Williams, G. & Watts, D. C. Non-symmetrical dielectric relaxation behaviour arising from a simple empirical decay function. *Transactions of the Faraday Society* **66**, 80-85, doi:10.1039/TF9706600080 (1970).
35 Schindelin, J. *et al.* Fiji: an open-source platform for biological-image analysis. *Nat Meth* **9**, 676-682,

doi:http://www.nature.com/nmeth/journal/v9/n7/abs/nmeth.2019.html - supplementary-information (2012).
36 Octopus 8.7.
37 Avizo, Fire 8.1.
38 Matlab R2015a.
39 Roylance, D. Engineering viscoelasticity. *Department of Materials Science and Engineering–Massachusetts Institute of Technology, Cambridge MA* **2139**, 1-37 (2001).
40 Derombise, G., Vouyovitch Van Schoors, L., Messou, M.-F. & Davies, P. Influence of finish treatment on the durability of aramid fibers aged under an alkaline environment. *Journal of Applied Polymer Science* **117**, 888-898, doi:10.1002/app.31534 (2010).
41 Merline, D. J., Vukusic, S. & Abdala, A. A. Melamine formaldehyde: curing studies and reaction mechanism. *Polym J* **45**, 413-419 (2013).
42 Abdelrahim, M. Y. M., Benjamin, S. R., Cubillana-Aguilera, L. M., Naranjo-Rodríguez, I., de Cisneros, J. L., Delgado, J. J., & Palacios-Santander, J. M. . Study of the electrocatalytic activity of cerium oxide and gold-studded cerium oxide nanoparticles using a Sonogel-Carbon material as supporting electrode: electroanalytical study in apple juice for babies. *Sensors* **13**, 4979-5007 (2013).
43 Cesano, F., Bertarione, S., Scarano, D., Spoto, G. & Zecchina, A. Designing of carbon nanofilaments-based composites for innovative applications. *Diamond and Related Materials* **18**, 979-983, doi:http://dx.doi.org/10.1016/j.diamond.2008.11.011 (2009).
44 Fukuda, M. & Kawai, H. Effect of Water on the Crystal Structure of Regular Kevlar. *Sen'i Gakkaishi* **52**, 582-590, doi:10.2115/fiber.52.11_582 (1996).
45 Fukuda, M. & Kawai, H. Moisture sorption mechanism of aromatic polyamide fibers. V: Growth of crystallites in as-spun wet poly(p-phenylene terephthalamide) fiber during dehydration. *Journal of Polymer Science Part B: Polymer Physics* **35**, 1423-1432, doi:10.1002/(SICI)1099-0488(19970715)35:9<1423::AID-POLB12>3.0.CO;2-8 (1997).
46 Kawabata, S. Measurement of the Transverse Mechanical Properties of High-performance Fibres. *The Journal of The Textile Institute* **81**, 432-447, doi:10.1080/00405009008658721 (1990).